TURUN YLIOPISTON JULKAISUJA
ANNALES UNIVERSITATIS TURKUENSIS

SARJA - SER. A I OSA-TOM.
ASTRONOMICA-CHEMICA-PHYSICA-MATHEMATICA

MAGNETIC PEROVSKITES Sr_2FeMoO_6 and $La_{1-x}Ca_xMnO_3$: SYNTHESIS, FABRICATION AND CHARACTERIZATION OF NANOSIZED POWDERS AND THIN FILMS

by

Tanja Suominen

TURUN YLIOPISTO
Turku 2009

From the Wihuri Physical Laboratory
Department of Physics
University of Turku
Turku, Finland
and
Graduate School of Materials Research
Turku, Finland

Supervised by

Professor Petriina Paturi and Professor Reino Laiho
Wihuri Physical Laboratory
Department of Physics
University of Turku
Turku, Finland

Reviewed by

Prof. Maarit Karppinen
Laboratory of Inorganic and
and Analytical Chemistry
Helsinki University of Techonology
Kemistintie 1
FIN-02015 Espoo
Finland

Dr. Roland Mathieu
Department of Engineering Sciences
Ångström laboratory
Division of Solid State Physics (FTF)
Uppsala University, Box 534
SE-751 21 Uppsala
Sweden

Opponent

Dr. Luise Theil Kuhn
Risø National Laboratory for Sustainable Energy
Technical University of Denmark
Frederiksborgvej 399
DK-4000 Roskilde
Denmark

ISBN 978-951-29-4152-0
ISSN 0082-7002

Acknowledgments

This work has been carried out in the years of 2004–2008 in the Wihuri Physical Laboratory at the Department of Physics and Astronomy, University of Turku. Graduate School of Materials Research and Jenny and Antti Wihuri Foundation are acknowledged for financial support.

Pori, November 2009
Tanja Suominen

Abstract

In this work a new method for preparation of Sr_2FeMoO_6 (SFMO) is studied. The citrate-gel method results in smaller grainsize for powders, better ordering in the structure and less parasitic phases than what is observed with other methods. Also, targets for SFMO thin film ablation were made with this method. The structural properties of powders and thin films were investigated using x-ray diffraction (XRD), atomic force microscopy (AFM) and scanning electron microscopy (SEM). For magnetic investigations, superconducting quantum interference device (SQUID) magnetometry, electron paramagnetic resonance (EPR) and Mössbauer spectrometries were used. The SFMO powder preparation procedure as well as the thin film ablation parameters are optimized.

The most critical parameters in obtaining a pure, structurally correctly ordered and preferably nanosized SFMO powder are the pH value of the solution before the heat treatment, and the reducing atmosphere and a suitable temperature during the calcination.

SFMO can have two different structures depending on the preparation conditions, i.e. the pH value and calcination temperature, which affect the grainsize and thus the structure. A tetragonal I4/m structure can be broken into a less symmetrical monoclinic P 2_1/n structure. As a size dependent feature, superparamagnetism is observed in SFMO powder samples with an average grainsize of approximately 30 nm.

Thin films were made using pulsed laser deposition (PLD). SFMO was ablated on two different substrates, $SrTiO_3$ and MgO. The films were completely c-axis oriented and no impurity phases could be observed from the films made with optimized ablation parameters. Ablation temperature plays the key role in obtaining pure and fully texturized SFMO films. Also, the pressure and using a comparable atmosphere during ablation as for powder calcination affect the film quality and the presence of impurity phases. With the target prepared by the citrate-gel method, the optimal ablation temperature could be lower and the ablation pressure could be higher than previously reported.

In this work $La_{0.9}Ca_{0.1}MnO_3$ (LCMO) thin films prepared by PLD were also studied. After preparation the films were annealed in oxygen and in vacuum, and the changes in structural and magnetic properties were studied by XRD, AFM and SQUID magnetometry. Photoinduced persistent magnetization (PPM) is observed when the films are illuminated with an Ar ion laser ($\lambda = 514$ nm (2.42 eV)). All films show magnetic cluster glass properties with a freezing temperature around 45 K.

Such a low doped LCMO is in the phase separation region where ferromagnetic and antiferromagnetic phases compete. The structural and magnetic properties are sensitive to the oxygen content changes, which are caused by the post-deposition treatments. Vacuum treatment leads to oxygen reduction which expands the lattice. The unpaired electrons are trapped in the formed vacancies, and these trapped electrons create rigid self-trapped magnetic polarons in the potential wells of local moments. Extra oxygen introduced into the lattice during oxygen treatment contracts the unit cell due to the oxidation of Mn^{3+} to Mn^{4+}. In comparison to the as-grown films, vacuum treatment enhances the magnetization values remarkably, whereas oxygen treatment roughly doubles the values. PPM measurements further clarify the changes in the electronic structure and the role of the oxygen vacancies that cause these changes in low-doped LCMO.

Preface

This thesis is based on the experimental work carried out at the Wihuri Physical Laboratory, Department of Physics, University of Turku during the years 2004-2008. The thesis consists of an introductory part and the following publications:

P1. J. Raittila, T. Salminen, T. Suominen, K. Schlesier, P. Paturi: *Nanocrystalline* Sr_2FeMoO_6 *prepared by citrate-gel method*, Journal of Physics and Chemistry of Solids **67**, 1712 (2006).

P2. T. Suominen, J. Raittila, T. Salminen, K. Schlesier, J. Lindén, P. Paturi: *Magnetic properties of fine SFMO particles: Superparamagnetism*, Journal of Magnetism and Magnetic Materials **309**, 278 (2007).

P3. T. Suominen, J. Raittila, P.Paturi *Pure and fully texturized* Sr_2FeMoO_6 *thin films prepared by pulsed laser deposition from target made with citrate-gel method*, Thin Solid Films **517**, 5793 (2009).

P4. T. Suominen, H. Huhtinen, S. Majumdar, P. Paturi, V. S. Zakhvalinskii, R. Laiho: *Persistent photoinduced magnetization and oxygen non-stoichiometry in* $La_{0.9}Ca_{0.1}MnO_3$ *films*, Journal of Physics: Condensed Matter **21**, 266001 (2009).

Papers relevant to this work but not included in the thesis

1. T. Suominen, P. Paturi, H. Huhtinen, L. Heikkilä, H.-P. Hedman, R. Punkkinen and R. Laiho: *Conductivity and distribution of charge on electroluminescent* Si/SiO_2 *structures investigated by electrostatic force microscopy,* Applied Surface Science,**222**, 131, 2004
2. J. Lahti, A. Savolainen, J. P. Räsänen, T. Suominen and H. Huhtinen: *The role of surface modification in digital printing on polymer coated packaging boards,* Polymer Engineering and Science, **44**, 2052, 2004.
3. M. Meretoja, R. Punkkinen, H.-P. Hedman, L. Heikkilä, M. Hirvonen, T. Suominen and M. Heinonen: *Electroluminescence in* Si/SiO_2 *microstructures,* Physica Scripta, **T114**, 53, 2004.

My contribution to the publications above is as follows: I made the AFM measurements and analysis, and participated in the XRD analysis in P1. I prepared the samples and made the XRD and magnetic measurements and analyzed the data apart from the EPR and Mössbauer measurements in P2. I prepared the targets and films, measured and analyzed the results in P3. I made the magnetic measurements in P4. I wrote papers P2-P4.

Contents

1 Introduction

1.1 Background to tunneling and colossal magnetoresistance

Tunneling magnetoresistance (TMR) was first observed in a layer structure, where between two Co-layers there was a Ge-layer [1]. Thirteen years later giant magnetoresistance (GMR) was observed in Cu/Co/Cu/Co and Fe/Cr/Fe multilayer structures [2, 3]. This observation soon led to magnetic storage devices in the markets. Yet stronger magnetoresistive behavior was observed in 1994 in a manganite material ($La_{0.67}Ca_{0.33}MnO_x$, LCMO) and was reported in a paper titled *Thousandfold Change in Resistivity in Magnetoresistive La-Ca-Mn-O Films* [4]. The observed MR was so much stronger than the giant magnetoresistance that it needed a new name to describe it, thus it was called colossal magnetoresistance (CMR).

In Fig. 1 is shown the tunneling magnetoresistant behavior of a layer structure, where the resistance changes as the applied magnetic field changes. Without external magnetic field, the magnetic layers are antiferromagnetically ordered. The layer in between the metals is a so-called tunneling barrier. Without an applied field, tunneling through the barrier is difficult because the spins of the electrons on both sides of the barrier point in different directions, thus the resistance is high. When an external magnetic field is applied, both layers have spin directions parallel to each other. This makes the spin dependent tunneling easier and the resistance gets lower. The steps are caused by the different coersive fields of the materials. It is to be noted that the GMR effect is obtained with the layered structure of materials with different strength of magnetization, whereas CMR is an intrinsic property of a material.

The mechanism of the CMR effect is related to super exchange (SE) [5] and double exchange (DE) [6] interactions, for example in Mn–O–Mn chains. In the SE interaction, the two electrons of the oxygen atom form a very strong antiferromagnetic or ferromagnetic coupling with the neighbouring Mn ions, which otherwise could not have direct interactions because of the distance (Fig. 3). Generally for Mn^{4+}–O–Mn^{4+} the interaction is antiferromagnetic, but for Mn^{3+}–O–Mn^{3+} it could be either ferro- or antiferromagnetic [7]. The bond resembles covalent bonding. In DE interactions the electrons actually move via the intermediate oxygen atom in the Mn^{3+}–O–Mn^{4+} chain. The movement is easy because the electron does not have to change its spin direction in order to get forward, while

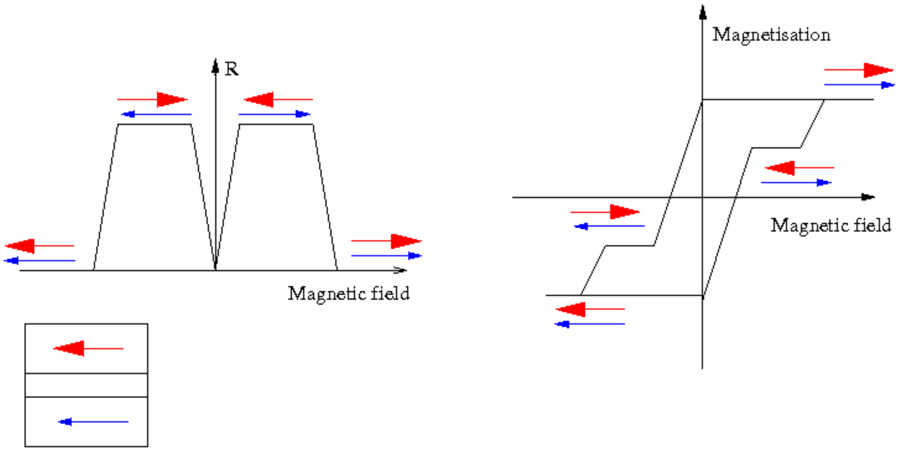

Figure 1. Schematic picture of the magnetoresistance and magnetization as a function of applied magnetic field in a layered structure. On the left side is shown the resistance changes as a function of applied magnetic field and on the right side the magnetization in an external field. Small image represents a layer structure in which two magnetic layers are separated by a non-magnetic layer, the upper layer having a stronger magnetisation than the bottom layer, therefore steps are formed in the magnetization picture. The strength and direction of the magnetic moments are shown with arrows in the pictures.

a valence difference is needed between the Mn ions for electrons to be able to move.

1.2 Sr_2FeMoO_6

The structure of Sr_2FeMoO_6 (SFMO) has been studied already in the 1960's [8], but a new boost for the study of the electronic and magnetic structure of the material started when Kobayashi *et al.* observed low field magnetoresistance (LFMR) in SFMO in 1998 [9]. LFMR is observed in polycrystalline samples, typically at the 0–0.1 T field range [7]. It is related to the ferromagnetic domains aligned in the magnetic field and can reach relative values of 50 % at low temperatures. LFMR differs from the intrinsic CMR as it is attributed to spin-dependent electron tunneling through the grain boundaries. The intrinsic CMR usually needs large external magnetic fields, up to few teslas, thus the name high field magnetoresistance, HFMR. Normally the MR is strongest near the Curie

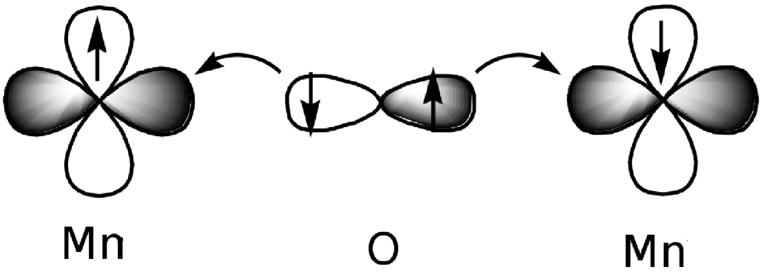

Figure 2. Schematic picture of the superexchange interaction in an antiferromagnetic Mn–O–Mn chain.

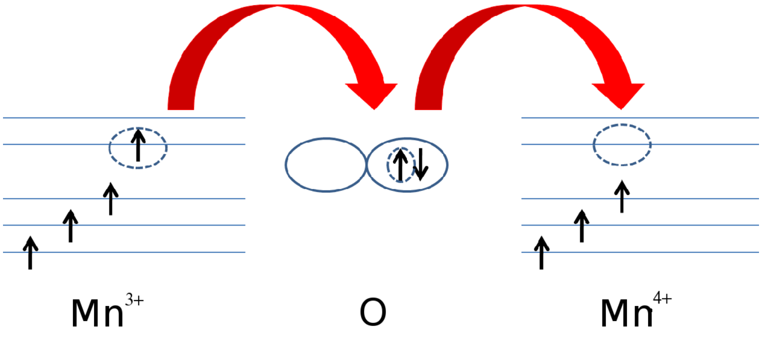

Figure 3. Schematic picture of the double exchange interaction in a Mn^{3+}–O–Mn^{4+} chain.

temperature, T_C, therefore the high-T_C materials are of great interest [7].

1.2.1 Structure and properties

SFMO is a half metallic ferrimagnet, which means that the conduction electrons are 100 % spinpolarized. Transport properties are dominated by spinpolarized tunneling through insulating grain boundaries, intergrain tunneling magnetoresistance (ITMR). ITMR is greatly enhanced with a smaller SFMO grainsize. Also, SFMO has very high Curie temperature (T_C). These properties are related to the grainsize of SFMO.

SFMO is sensitive to water and air and will completely decompose in interaction with water. When SFMO is heated in air, the Mo-ions will evaporate [10]. An ageing effect has been observed and studied in sintered pellets and thick films [11]. In sintered pellets the unit cell expansion and decomposition to $SrMoO_4$ is rather moderate in air at room temperature. In both reports the samples were prepared by solid state method. Both effects were stronger on screen printed thick films [11].

SFMO has a double perovskite $A_2BB'O_6$ structure, where A is an alkali earth metal, B and B' are heterovalent transition metals. The Fe and Mo atoms are inside an oxygen octahedron (Fig. 4) and the large Sr atoms are positioned in the center of each cube formed by the octahedra. In the optimal structure, the Fe and Mo atoms would be in an alternating order like in NaCl. Often it happens that Fe is replaced by Mo and vice versa. This is called B-site disorder or antisite (AS) disorder. It is also possible that the iron atoms form a row in the structure which acts as a boundary between two phases in the structure due to the stronger antiferromagnetic coupling between Fe–O–Fe bonds than the coupling between Fe–O–Mo. These are shown schematically in Figure 5 A-C and will be discussed later in detail.

The B-cation octahedron in the double perovskite structure can be arranged in three different ways (randomly, rock salt type alternating order, or layered). The arrangement type depends primarily on the charge difference between the B and B' cations and secondarily on the size difference of the cations, also the A-site cation in the middle affects the type of B-site cation arrangement. For double perovskites to form the rock salt type order at the B-site, the ionic radius difference between B+B'- and A- cations should be less than 0.2 Å, and the charge difference between B and B' cations 2 or more [12]. The ionic radii of the

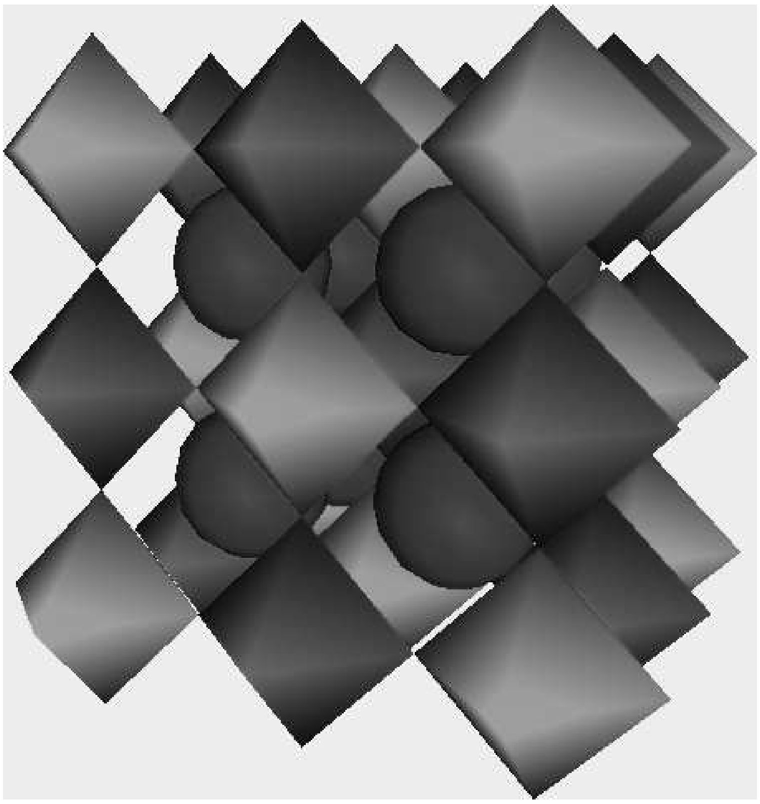

Figure 4. Schematic picture of the SFMO unit cell structure. Inside the octahedron is either a Fe or Mo atom, alternating, and at each corner of an octahedron is an oxygen atom. The Sr atoms are positioned inside the cubes.

Table 1. The ionic radii of the ions in SFMO [13].

Ion	Fe^{2+}	Fe^{3+}	Fe^{4+}	Mo^{5+}	Mo^{6+}	Sr^{2+}	O^{2-}
r (Å)	0.78	0.65	0.59	0.61	0.59	1.32	1.40

ions in the SFMO are shown in Table 1.

A lot of work has been done on AS defects and disorder study, the theoretical [14] and experimental [15] results being in good agreement with each other. The net magnetization, M_{sat}, of SFMO decreases linearly from the theoretical value 4 μ_B/formula unit (f.u.). with the increase of AS disorder and follows the rule $M_s = (4 - 8x)\mu_B$/f.u., where x is the fraction of Fe atoms replaced by Mo [14, 15]. The Fe–O–Fe interaction is strongly antiferromagnetically coupled, thus reducing the total magnetization caused by the Fe atoms (Fig. 5 A), whereas the misplaced Mo in Mo–O–Mo is paramagnetic and does not compensate the magnetization reduction caused by a misplaced Fe -atom [14, 16, 17]. Similarly the T_C and the MR effect are lowered by the AS disorder.

Highly disordered SFMO is no longer half metallic and does not have any LFMR response, though the high field MR is not affected by the AS disorder [16, 18]. This can be understood by the difference of the mechanisms, for LFMR depends on the half metallic ferromagnetism and is caused by the intergrain spin-dependent scattering of the highly spin polarized charge carriers, whereas the high field MR has an intragrain origin [18].

The AS ordering can be controlled by the preparation parameters, such as the sintering time and temperature. As a rule of thumb it could be said that the higher the temperature, the better the ordering [15, 19] although too long sintering times result in several impurity phases [20]. This rule is valid only at sintering temperatures below 1200°C, at higher temperatures the ordering decreases with the increased temperature [21, 22].

In [16] it was concluded that the AS disorder would not be only point defects as shown in Fig. 5B, but the structure would be more disturbed. These larger disordered chains or areas are called antiphase boundaries (APB), shown in Fig. 5C and have been observed with high energy electron microscopy [23].

The degree of ordering is not the only thing to affect the MR properties, the grain size plays an important role as well. Smaller grain sized SFMO still

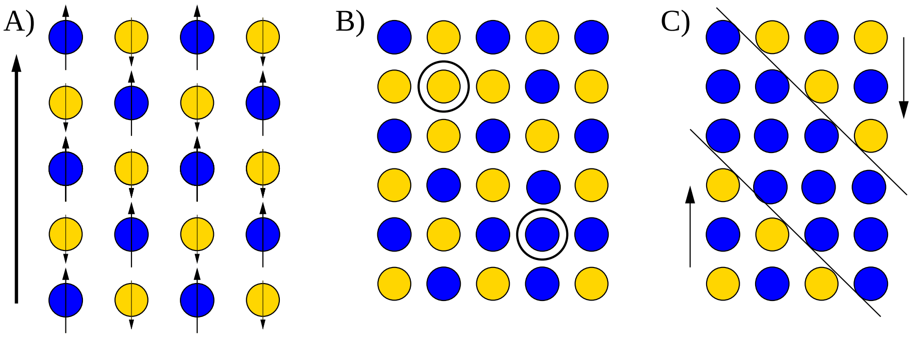

Figure 5. Schematic picture of the structure SFMO described by Fe (dark) and Mo (light) atoms. In A) the ideal ordering of the structure is shown. Arrows represent the magnetic moments of Fe (up) and Mo (down), total magnetization being on the direction of the Fe -atoms. This is type G antiferromagnetism [27]. B) shows the antisite disorder as a point defects of single Fe or Mo atoms misplaced in the structure (circled). C) shows the antiphase boundary (APB), which is formed by misplaced Fe -atoms. Both sides of the boundary are antiferromagnetically ordered (A), but their total magnetic moments point in opposite directions. The APB can also be only two Fe-layers thick [28, 29].

has better MR values than better ordered, but larger grain size SFMO [23]. The lattice parameters do change as a result of the AS disorder, but not enough to tell the difference between ordered and disordered samples [17, 18]. The degree of AS order can be estimated from the superstructure peaks and their intensities on the x-ray diffraction data, for example $I(101)/(I(200) + I(112))$ [17, 18, 24]. Rietveld refinement can be used for determination of the AS order from the XRD data by setting the Fe/Mo occupancies as one of the parameters to be refined [24],[**P1**],[**P2**].

SFMO is reported to have two different structures, either cubic $Fm\bar{3}m$ or tetragonal $I4/mmm$. The change of the structure is related to the Fe/Mo - ordering and stoichiometry. Fe rich SFMO ($Sr_2Fe_{2-x}Mo_xO_6$) has a cubic structure when $x > 1.2$ [25, 26]. Although the Fe^{3+} ionic radii is larger than the Mo^{5+} (Table 1), the lattice parameter contraction is observed due to the valence and vacancy disproportion.

When the LFMR was first found in SFMO [9], the MR effect was described with a rather simple model involving the antiferromagnetic coupling between the

Fe^{3+} (S=5/2) and Mo^{5+} (S=1/2) cations bridged by an oxygen atom. This gave the theoretical value of total magnetization of SFMO to be 4 μ_B/f.u. Later on, when this theoretical value was not reached, it was realized that this model is far too simple to describe the magnetism in SFMO.

It has been shown that the Fe valence varies between Fe^{2+} and Fe^{3+} in the structure [30, 31]. This mixed valence is an indication that there are itinerant electrons in the structure. These make two types of magnetic interactions possible in the structure, the antiferromagnetic interaction between the FeO_6 and MoO_6 sublattices and a double exchange type charge transfer in Fe^{2+}–O–Mo–O–Fe^{3+} involving the itinerant electrons [32]. Because of the itinerant electrons the saturation magnetization cannot reach 4 μ_B/f.u. even in ordered SFMO but decreases to 3.5 μ_B. According to this new theory, the dependence of M_s on the AS disorder changes to $M_s = (3.53 - 3.56)x$ μ_B/f.u., which is in even better accordance with the experimental results than the previous one [32]. On the other hand, after this model was developed, nearly ideal magnetization values have been reported (¿ 3.95μ_B/f.u.) [33], which is higher than the model predicts.

The new model is built on the itinerant electrons in the structure and it is supported by the studies related to the AS disorder and confirmed with the experiments on SFMO doping. Normally there is 1 itinerant electron/ f.u. originating from the Mo cation. When the Mo cation is replaced by W^{6+} (hole doping), there are no itinerant electrons and the structure changes from half metallic ferrimagnet to an insulator without any long range magnetic ordering [34].

1.2.2 Doping

In Figure 6 are shown the elements, which are used either in forming of similar $A_2BB'O_6$ double perovskite structures as SFMO or for doping the SFMO structure via substitution. After the discovery of LFMR in SFMO, other similar $A_2BB'O_6$ double perovskite structures have also been studied. Change on A-site: Ca_2FeMoO_6 [37, 38, 41, 42], Ba_2FeMoO_6 [42, 53], change on B-site: Sr_2CrMoO_6, Sr_2CoMoO_6 and Sr_2MnMoO_6 [43] and B'-site: Sr_2FeRuO_6 [27], Sr_2FeWO_6 [55]. For studies of the SFMO electronic structure, La has been used for Sr substitution for electron doping [40, 44], similarly hole doping effects have been studied by Ba substitution for Sr [52] and W substitution for Mo [34, 39, 56]. Magnetic properties have been studied with the Sr substitution with magnetic atoms such

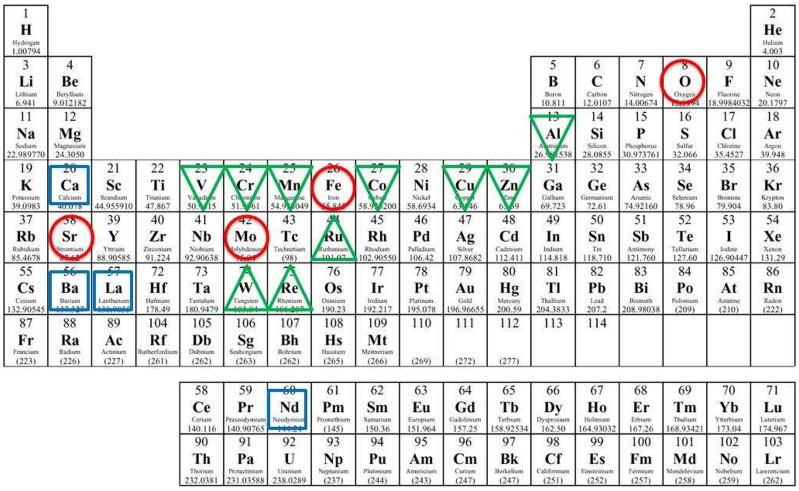

Figure 6. SFMO elements are marked with circles. Squares are the elements that are used on A sites and/or used to subsitute Sr in SFMO, inverted triangles mark the B-site elements and/or elements used for substitution of Fe in SFMO, triangles are for B’ elements and/or are used for Mo substitution. Data is collected from [27, 34–54]

as Nd [50] and Fe substitution with non-magnetic atoms such as Al [49]. Other dopants that are used to gain a better understanding of the properties and structural matters e.g. B-site ordering, antiphase boundaries and their formation are Ca for Sr [46, 47], Fe substitution with Mn [45], V [48], Zn [51], Ni [57] and Cr [54]. All these studies have helped to increase the understanding of the SFMO properties.

1.2.3 Preparation methods

The preparation of SFMO can be divided mainly into two categories of methods: the solid state method and wet-chemistry methods including sol-gel and citrate-gel methods. In the first, starting ingredients are in a powder form and these powders are thoroughly ground and mixed before heat treatments [58–63]. Wet-chemistry methods [36, 64–68] differ from the solid state methods in that the starting materials are mixed to form a solution, which is then dried before the heat treatments. The recipes can vary in both methods and especially the heat treatment temperature, duration and gas flow are parameters that vary greatly. The whole process depends on those variables, e.g. the purity of SFMO and the quality of obtained SFMO.

Usually used ingredients in the solid state method are $SrCO_3$, Fe_2O_3 and MoO_3 [10, 69, 70], but other starting compounds have also been used [63]. Stoichiometric amounts of these powders are mixed and they form $SrMoO_4$ and $SrFeO_{3-x}$, SFMO is formed via substitution of Mo to $SrFeO_{3-x}$ [69].

For wet-chemistry methods, the nitric-acid based method [65, 67, 71] and citric acid based method [66] are used. Stoichiometric amounts of starting ingredients are mixed with either of the acids forming a homogeneous solution. The starting compounds for the nitric acid method can be $(NH_4)_6Mo_7O_{24}\cdot 4H_2O$, $Fe(NO_3)_3\cdot 9H_2O$ and $Sr(NO_3)_2\cdot 4H_2O$ [65, 71] and for the citric acid method the $Fe(NO_3)_3\cdot 9H_2O$ is replaced with $FeC_2O_4\cdot 2H_2O$ [66], [**P1**].

There are several differerences between these two types of preparation methods. The sol-gel method is faster than the solid state method, although in principle solid state method seems simpler. The thorough grounding at the beginning can already take several days [20, 70].

The sol-gel method on the other hand is more complex with mixing all the ingredients. The advantages of the wet chemistry methods are that the solution is homogenously mixed on the atomic level and the SFMO is already pre-formed and Fe-Mo order is developed, even before the calcination and sintering takes place (comparison to SFMO formation via Mo-substitution during synthesis with the solid state method, when disorder is much more likely to occur).

The solid state method requires higher calcination and sintering temperatures, as well as a longer sintering time than wet-chemistry methods.

Maybe the most important difference is in the resulting SFMO powder itself. With the solid state method it is impossible to reach such a small grainsize which is formed inevitably with the sol-gel method. From a solid state reaction the obtained SFMO grainsize is up to several micrometers. With the more controlled wet-chemistry methods the grainsize stays on the nanometer scale, which becomes an important factor when considering for example thin film ablation.

1.2.4 Thin film preparation methods

There are several different methods and options that are used for SFMO thin film preparation. In the next section these methods are shortly described and the advantages and disadvantages related to them are discussed.

SFMO thin films have been prepared *in situ* on $LaAlO_3$ substrates via a chemical vapour process, ultrasonic spray pyrolysis (USP) [72]. This method has the nature of the wet-chemistry method. First, the starting solution is prepared as described in the previous section. This aqueous solution, containing dissolved Sr and Fe nitrates and ammonia complexed molybdic acid, is then formed into a mist by introducing the solution vessel into an ultrasonic bath in which vibrations creates the mist. A heated substrate is positioned above the vessel. The created mist is transferred from the vessel to the substrate surface, $Ar/H_2(5\%)$ being the carrier gas. The deposition rate is approx. 100 Å/min. During deposition the substrate temperature is 600 – 900°C. Deposition, which takes half an hour, is followed by postannealing at 1200°C for 5 hours in the same gas flow as used during deposition. With this method it is possible to cover large areas, the preparations for deposition is simple and the method does not require vacuum conditions.

Another wet-chemistry type method for thin film preparation is a chemical solution deposition (CSD) [73, 74] in which the concentrated starting solution is spin coated on the substrate and the solution preparation route is optimized. Again the actual SFMO formation takes place on the substrate surface during several heat treatments. At first the film is heat treated at 400 °C for 1 hour, then one hour in an oxygen flow at 750 °C and finally treated in a reducing Ar/H_2 (0.7%) gas flow. Films with this method were made on $SrTiO_3$ (STO) and MgO (001) substrates.

Both above mentioned methods resulted in approximately 300 nm thick films.

Sputtering has been used on various substrate materials: $LaAlO_3$ (LAO), $SrTiO_3$ (STO), MgO and $Sr_{0.5}Ba_{0.5}TiO_3$ [75]. The sputtering was made on heated substrates in an Ar- atmosphere. Results were substrate dependent and on MgO and LAO -substrates it was observed that when the film thickness was reduced to 30 nm they changed to be more Fe rich and Mo deficient. A similar effect was not observed on other substrate types. Several impurity phases were detected and identified on each film grown with this method. For thinner films the identified impurities were more iron based and for thicker films more $SrMoO_4$ was detected, probably an indication of Fe rich SFMO grains.

The most used and optimized method for SFMO thin film preparation is pulsed laser deposition (PLD) [58–61, 76–86]. In this method the target is already pure, stoichiometric SFMO, prepared either using the solid state method (micron grained targets) or wet-chemistry methods (nanograined targets) [**P3**].

The preparation method used for the target is in a keyrole, since the grainsize of the used target directly affects the quality of the films and the parameters needed to obtain that quality. Also studies on $YBa_2Cu_3O_{6+x}$ films clearly show that the films made from nano-targets have better properties in comparison to the films made from a target with micron sized grains [87, 88]. Therefore the nanograined target is more preferable also when this method is used for the SFMO film preparation.

The target is introduced into an ablation chamber. The heated substrate is positioned so that when the laser hits the target and creates the plume, the plume hits the substrate. At this point it is important that the target – substrate distance is correct and just the tip of the plume touches the substrate.

Inside the ablation chamber is a low pressure gas-atmosphere, either an oxygenating atmosphere with O_2 present [58–60, 77, 79–81, 85, 86] or a reducing Ar/H_2 atmosphere [59, 60]. The challenge with this method for SFMO thin film preparation is that it requires low pressure and rather high substrate temperatures in order to obtain good quality. Pure films and different ablation routes have been developed from one step to many step growth processes, and several different heat treatments have been tried, pre-annealing, during annealing and post-annealing methods.

Several impurities have still been observed from the films, such as $SrMoO_3$, $SrMoO_4$, Fe_2O_3, Fe_3O_4, Fe and an unknown yellowish phase [58–62, 75, 79, 80]. Main problems are the easily formed impurity phases, and the secondary problem to obtain the ordered SFMO structure. A lot of work has been carried out in order to find the optimal ablation temperature, atmosphere and pressure for SFMO thin films. Moreover, each parameter affects the others and each combination can give films with completely different properties. The use of a nanograined target moderates the needed parameters considerably, e.g. temperature and pressure. Also the problems with the film quality and purity can be overcome with the use of a right kind of target [**P3**].

1.3 Manganites

1.3.1 Structure and properties

The mixed valence manganites $La_{1-x}M_xMnO_3$ with M = Sr, Ca, Ba have attracted much interest because of their colossal magnetoresistance behavior, high spin-polarization of the ground state and magnetic phase separation. The mag-

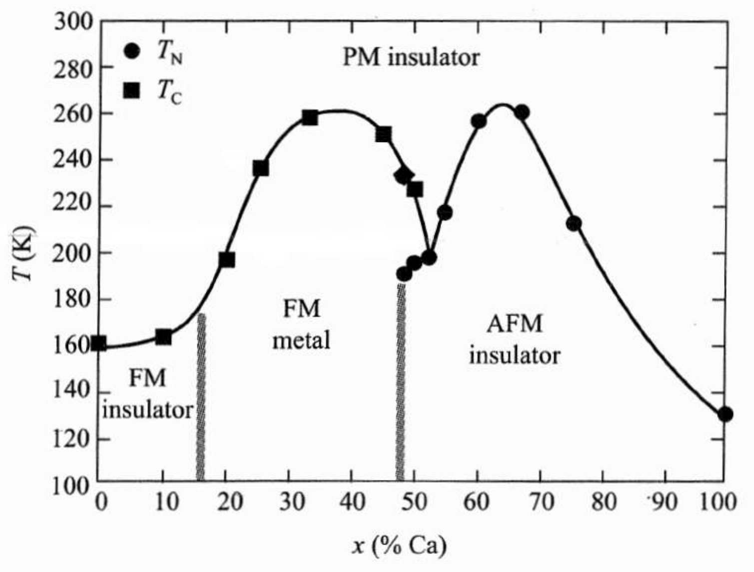

Figure 7. The magnetic phase diagram of LCMO [94].

netic phase diagram of the $La_{1-x}Ca_xMnO_3$ (LCMO) is shown in Fig 7. Recent studies show more complicated structures at low values of x. At x< 0.07 LCMO is an antiferromagnetic (AFM) insulator, between 0.07 < x < 0.22 an insulating ferromagnet (IFM) and for 0.22 < x < 0.5 a ferromagnetic metal (FMM). For x < 0.125 small metallic ferromagnetic (FM) clusters are embedded in the IFM phase as observed by NMR [89], neutron-diffraction [90] and magnetic measurements [91–93].

Manganites have a perovskite structure (Fig. 8(b)). This single perovskite structure is similar to the SFMO double perovskite, but in LCMO the octahedron contains an Mn -ion and the middle atom is either La or Ca. Mn and O ions form Mn^{3+}–O–Mn^{4+} chains in which the electrons moves from Mn^{3+} to Mn^{4+} via an oxygen atom [95]. The mechanism is strongly dependent on the oxygen stoichiometry in the structure [96]. The LCMO films grow on STO at 45 degree angle (Fig. 8(a)) in order to minimize the lattice mismatch effect.

Oxygen stoichiometry affects also the lattice parameters [97]. When oxygen is removed from the structure, the lattice expands due to the Mn valence changes whereas oxygen increase in the structure makes the lattice smaller, again due to the Mn ions. Annealing treatments can be used to vary the amount of oxygen in the structure [98]. As the magnetic properties of LCMO are dependent on

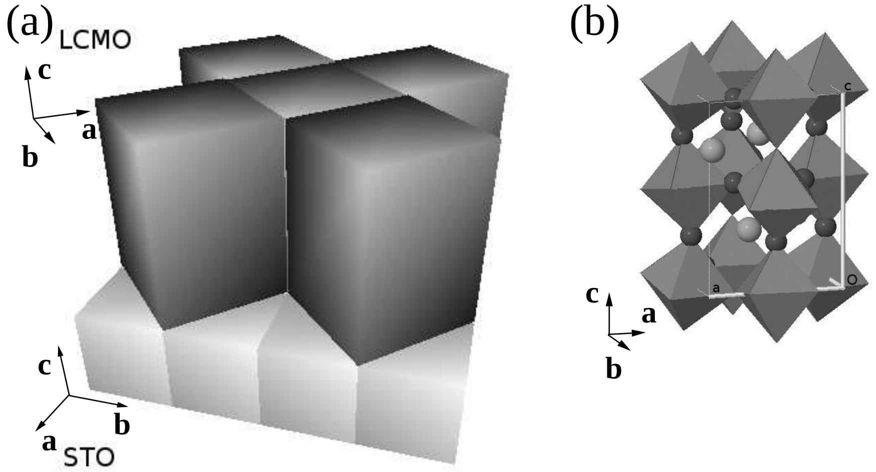

Figure 8. (a) Schematic presentation of the orthorhombic structure of LCMO film on (001) STO and (b) unit cell of LCMO [**P4**].

the electron hopping in Mn–O–Mn chains, they are also dependent on oxygen stoichiometry.

1.3.2 Photoinduced magnetization in $La_{1-x}Ca_xMnO_3$

An increase of the FMM phase was observed at low temperatures under illumination with red light [99]. This induced magnetization decayed slowly after the light was switched off. This persistent photoinduced magnetization (PPM) [100] resembles the persistent photoinduced superconductivity in low-doped $YBa_2Cu_3O_{6+x}$ [101]. The main optical absorption bands of LCMO are due to the $3d(t_{2g}) \rightarrow 3d(e_g)$ excitations with maximum around 1.5 eV and the $2p(O) \rightarrow 3d(Mn)$ charge transfer transition around 2.4 eV [102]. The increase of the Mn^{4+} ions under illumination can be expressed as $Mn^{3+}+Mn^{3+}+h\nu \rightarrow Mn^{4+}+Mn^{2+}$. The number of Mn^{3+} ions on the other hand decreases under illumination as has been observed from Mn^{3+} core level spectra measurements [103].

2 Experimental details

2.1 Experimental methods

2.2 X-ray diffraction

X-ray diffraction (XRD) measurements were made with a Bragg-Brentano-type Phillips Xpert Pro MPD set up with a Cu-anode and a reflected beam monochromator tuned for CuK_α. The sample holder for 2θ-scans on powder samples was a copper plate with a machined sample space. For film samples, a Schulz texture goniometer, which allows also sample rotation ϕ and sample tilt ψ, was used (Fig. 27) [104].

The powder XRD patterns were refined with the FULLPROF Rietveld refinement program [105]. The Thompson-Cox-Hastings (TCH) pseudo-Voigt peak profile function [106] was used and parameters for the instrument function were obtained from a refinement of an Al_2O_3 standard. The spacegroup I 4/m with structural data by Chmaissem *et al.* [107] was used as a starting point for SFMO refinements. The refined parameters were zeropoint, background, scale, lattice parameters, peak width parameters, Mo/Fe site occupancy (antisite disorder) and general isotropic temperature factor. When a large amount of phases were refined, some of the parameters had to be fixed for phases with very few and low intensity peaks.

Texture measurements were made on SFMO thin films grown on STO and MgO substrates. Because the substrate peaks are dominant over the SFMO film peaks, the measured peak angles were carefully chosen to avoid overlapping with substrate peaks.

2.3 Microscopies (SEM, AFM)

AFM measurements were made with a Thermomicroscope AutoProbe CP Research AFM/STM/EFM system. Cantilevers were Anfatec's triangular contact and non-contact Si-tips with reflective coating. For the measurements included in this work, both contact and non-contact modes were used.

For SFMO thin film surface structure studies, a few SEM images were taken with a Cambridge S200 scanning electron microscope at 20 kV.

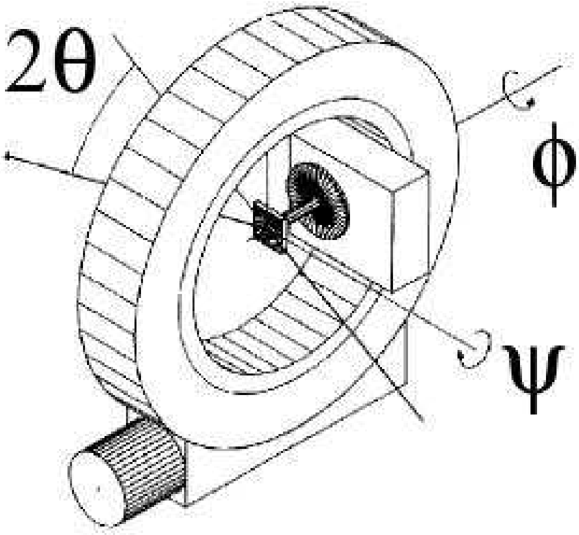

Figure 9. Schematic figure of the goniometer used in XRD measurements shows the 2θ, ψ and ϕ angles [108].

2.4 Investigations of magnetic properties

2.4.1 Magnetic measurements

Magnetization measurements were made with a Cryogenic Limited S600X SQUID magnetometer. Samples, powders and films, were sealed in Teflon tape pockets. Magnetic fields up to 4 T and temperatures ranging from 5 K to 300 K were used. With an extra oven temperatures as high as 580 K could be reached.

For the light induced magnetization an optical fibre was led from the Ar ion laser ($\lambda = 514.5$ nm (2.42 eV)) to the sample space. All these measurements were made first in the dark and then under illumination, without taking the sample out from the magnetometer between the measurements. The external field B was always oriented along the plane of the films, i.e. along the LCMO [110] axis.

2.4.2 Mössbauer spectroscopy, EPR

Ferromagnetic resonance measurements (FMR) were made with an X-Band EPR spectrometer (9.03 GHz) at temperatures from 10 K to 300 K.

Mössbauer measurements were made by Johan Linden at Åbo Akademi physics department.

Mössbauer absorbers were made by spreading the sample powder, mixed with an epoxy resin, on an Al foil. The absorber thickness was ~20 mg/cm^2 of SFMO. Spectra were recorded in a transmission geometry using the maximum Doppler velocity of 11.15 mm/s. The absorber temperatures were set at 77 K and at 6 K. Additionally, an external magnetic field of $B_{\text{ext}} = 0.6$ T was applied when re-measuring the superparamagnetic small-crystalline sample at 77 and 6 K. The direction of the applied field was perpendicular to the Mössbauer γ beam.

2.5 Sample preparation

2.5.1 Citrate-gel method

SFMO powder was prepared with the citrate-gel method. The starting materials were $Sr(NO_3)_2$ (99.9 %), $Fe(NO_3) \cdot 4H_2O$ (99.9 %), Mo powder (99.999 %) and citric acid monohydrate (99 %).

Instead of the usually used $(NH_4)Mo_2O_7$, the Mo solution was prepared by weighing accurately 4 g of Mo powder, which was first ground into a homogeneous fine powder and then mixed with a small amount of water. Released red brown gas, which might be NO_2, was observed when nitric acid was slowly added to the solution under stirring and heating. After 55 ml of conc. nitric acid was added and no more red brown gas escaped, the solution had turned into a white mash. Due to violent heating, ammonia (25 %) was added very carefully to the solution until the solution cleared. Finally, water was added to the slightly yellow solution until the exact volume was filled.

The SFMO solution was prepared by mixing water solutions of strontium and iron nitrates in a mole ratio of 2:1=n(Sr):n(Fe). Solid citric acid was added to the solution in a mole ratio of 6.5:1=n(citric acid):n(Fe). After this, the prepared Mo solution was added in the mole ratio 1:1=n(Mo):n(Fe). If the Mo solution was added before the citric acid, precipitation occurred. Ethylenediamine (EDA) was added under constant stirring until the wanted pH value was obtained. Several different pH values were studied from 1.5 to 9.0 with 1.5 steps.

All the samples were placed into an oven, where they were kept at 100°C for 22 hours. During the 22 hours, the two lowest pH samples swelled very strongly and the other samples transformed into gels. The temperature was risen to 150°C and after 20 hours all the samples had swollen very much and afterwards no more swelling was observed. Finally the temperature was raised to 200°C at which the samples were kept for 24 hours. The obtained black solid foams were ground and fired at 500°C for 2 h in air. The resulting light brown powders were lightly crushed, and they were the precursors for the following calcinations.

The precursors were measured with XRD, the present phases at this point of preparation were $SrMoO_4$, $SrCO_3$, Fe_3O_4 and $Sr(NO_3)_2$ (Table 2). The weight percent (wt%) and crystalline size D (nm) are obtained from the Rietveld refinement.

The precursors were calcined at 975°C and 1050°C for 38 h in Ar with 5% of H_2 flowing at a rate of 0.06 l/min. The samples were heated to the dwell temperature in 4 hours and furnace cooled in 4 hours to about 200°C. Calcination at 975°C results in better Fe-Mo order in the powders and less impurity phases. The pH value of 7.5 gives the best ordering at both calcination temperatures and the purest SFMO. Therefore, for the subsequent SFMO preparation we chose to prepare precursors from a solution with a pH of 7.5 and to calcinate at 975°C. The pH and calcination temperature effects can be seen in Table 2.

2.5.2 Film deposition

The SFMO powder was prepared using the citrate gel method as described in previous section. The powder was then pressed 5 minutes with a pressure of 150 MPa to a 20 mm diameter pellet, which was further calcined three times for 6 hours at 975°C and 12 hours at 1050°C in an Ar/H_2(5 %) gas flow.

Films were ablated on single crystalline (100) $SrTiO_3$ (STO) and (100) MgO substrates with a XeCl eximer laser (λ = 308 nm). The ablation set up is schematically shown in Figure 10. Ablation parameters such as the pressure and the substrate temperature were optimized. The best film quality was reached in a reducing atmosphere of Ar/H_2 (5 %). First, the chamber was flushed two times and the base pressure was adjusted to 10 Pa. The ablation temperature was from 780 to 880°C and the post-deposition annealing temperatures were from 860°C to 880°C. On both substrates the SFMO films were fully texturized and pure.

An Ar/H_2 (5 %) reducing gas mixture was chosen due to the earlier observation of its good effect during powder preparation. The same gas mixture has been used in SFMO film preparation previously, also the ageing effects of the films are small when prepared in this mixture [59]. The reducing gas mixture resulted in less impurities and a better ordering in the films. Optimal pressure during ablation was determined by analyzing the plume size and shape visually. The plume was best when the pressure in the ablation chamber was 10 Pa. At lower pressures the plume was small, more dispersed. At 10 Pa the plume had

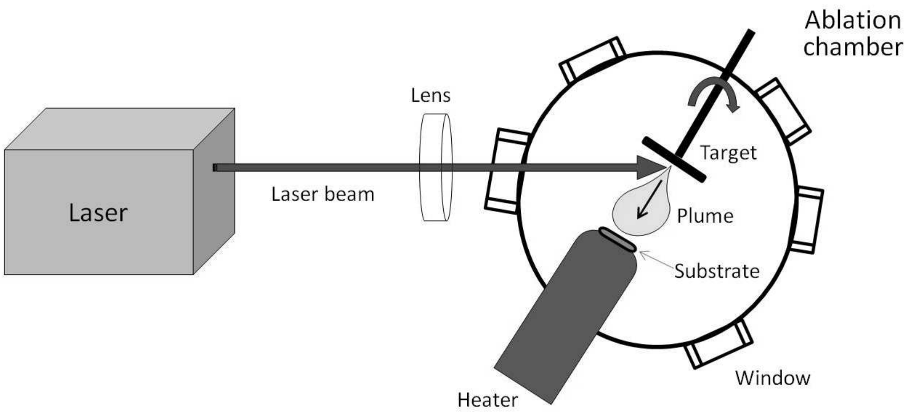

Figure 10. Schematic picture of the used ablation set up.

a nice shape and it was easy to adjust it to reach the target, the distance between target and substrate being 35 mm. At pressures above 10 Pa the plume got smaller and did not reach the substrate anymore.

LCMO films of 200 nm thickness were grown on (001) $SrTiO_3$ (STO) substrates by pulsed laser deposition (PLD) with the same ablation setup as was used for SFMO film preparation. In order to increase or decrease the oxygen content of the films, post-annealing treatments were made in flowing oxygen and in vacuum. The (001) STO substrate was chosen to obtain minimal lattice mismatch between the film and the substrate. Depending on Ca concentration x, the lattice mismatch in LCMO films with $x = 0.1$ grown on (001) STO is +0.5% with tensile strain, while in LCMO with $x = 0.33$ the mismatch is on average +1.0%.

3 Physical properties of the SFMO nanopowder prepared by the citrate-gel method

3.1 Grainsize and purity of the powders

3.1.1 XRD

The precursors and the calcined powders were analysed with X-ray diffraction (XRD).

The phases identified from the XRD patterns of the precursor powders are listed in Table 2 with the weight percent and the crystalline size of the phase. The major phase was $SrMoO_4$ in all the samples and other phases found are SFMO, $SrCO_3$, $Sr(NO_3)_2$ and Fe_3O_4. $Sr(NO_3)_2$ was found only in the sample prepared using the lowest pH and it had probably precipitated during the water evaporation. The peaks of $SrCO_3$ and $SrMoO_4$ clearly widen as the pH increases, indicating a reduction in the crystalline sizes, which is also the result of the refinements as shown in Table 2.

The six sets of precursor powders were calcined at 975°C and 1050°C to form the final SFMO powders. Final powders were measured with XRD and the data was analyzed with the Rietveld refinement, an example of the refined data shown in Figure 11. The crystalline size, D, ordering of the SFMO and recognized other phases are shown in Table 3.

The formation of SFMO is very pH dependent, and in the very low pH solutions, SFMO forms at lower temperatures. Already after the precursor preparation at 500°C some SFMO is observed. At first glance pH = 3.0 seems the most favorable for efficient SFMO production (Table 2), but the situation changes during calcination as the precursors made from the higher pH value solutions result in less impurity phases than the precursors from the more acidic starting solutions (Table 3). The purest final SFMO powders were obtained from the pH = 9.0 solution, although the antisite order was slightly lower than in the powders made from the pH = 7.5 solution. It can be concluded after comparison of the amount of impurities and the degree of ordering that the best quality SFMO powder was obtained from the pH = 7.5 solution.

The differences caused by the different calcination temperatures in the SFMO purity and antisite order are not as profound as in the crystalline size. The antisite order is significantly better in low-T samples, but in the pH = 7.5 and 9.0

Table 2. The observed phases in the precursor powders listed with the starting solution pH. The weight percent (wt%) and crystalline size D (nm) are given for the observed phases [**P1**].

	$SrMoO_4$		Sr_2FeMoO_6		$SrCO_3$		Fe_3O_4		$Sr(NO_3)_2$	
pH	wt%	D	wt%	D	wt%	D	wt%	D	wt%	D
1.5	46	78	22	15	10	69	6	20	16	≥ 200
3.0	44	14	38	9	12	28	5	23	0	
4.5	57	23	7	5	25	19	11	17	0	
6.0	57	16	4	9	30	17	9	9	0	
7.5	64	12	0		29	18	7	9	0	
9.0	64	9	0		24	12	12	4	0	

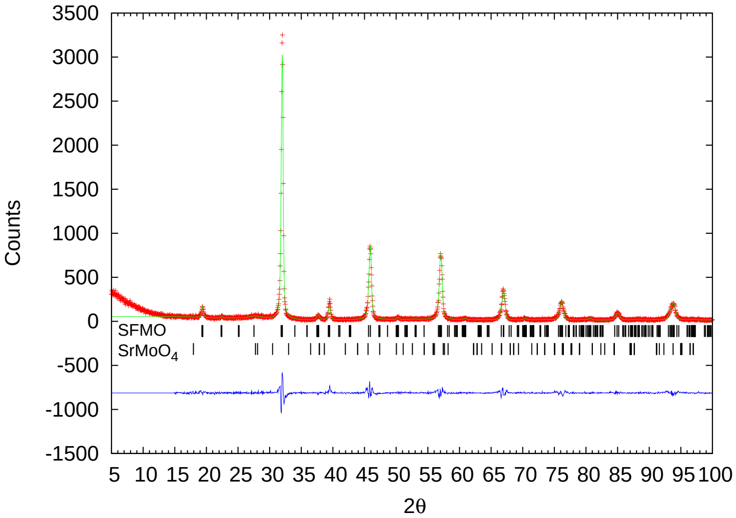

Figure 11. XRD measurement (crosses) and Rietveld refinement (line) for SFMO powder prepared from a pH = 7.5 solution and calcined at 975°C. Antisite disorder is 10 %, average SFMO grain size 31.1 nm and χ^2 for the refinement is 1.72. Line positions for SFMO and $SrMoO_4$ are shown below the data. $SrMoO_4$ causes a very broad peak around 27 degrees, the refined grainsize being 2.3 nm [**P2**]

Table 3. The contents of the samples calcined at 975°C and at 1050°C for 32 h at Ar/5% H_2. Also the crystalline size D and ordering of SFMO are given along with the Rietveld refinement goodness of fit indicator, $\chi^2 = (R_{\mathrm{wp}}/R_{\mathrm{exp}})^2$. The number in the parenthesis after a phase name is the weight percent of the phase, and in some cases a crystalline size is given.[**P1**]

			SFMO		other phases
975°C	pH	χ^2	D (nm)	order (%)	
	1.5	1.50	21	58	$SrMoO_4$(37), Fe_3O_4 (1)
	3.0	1.43	24	62	$SrMoO_4$(14)
	4.5	1.86	19	64	$SrMoO_4$(28), Fe_3O_4(2), $Sr(OH)_2$(1)
	6.0	1.57	24	76	$SrMoO_4$(13 D=3nm)
	7.5	1.72	31	90	$SrMoO_4$(8, D=2nm)
	9.0	1.62	30	80	$SrMoO_4$(6, D=2nm)
1050°C	pH	χ^2	D (nm)	order (%)	
	1.5	2.64	78	23	$SrMoO_4$(41), Fe_3O_4(2), FeO (4), unknown phase
	3.0	2.31	150	14	$SrMoO_4$(20)
	4.5	2.81	174	14	$SrMoO_4$(30), FeO(2)
	6.0	2.65	213	28	$SrMoO_4$(15)
	7.5	2.47	197	85	$SrMoO_4$(3)
	9.0	2.38	239	78	$SrMoO_4$(3), unknown phase

samples there is no difference between the 975°C and 1050°C calcined samples. The crystalline size is strongly affected by temperature regardless of the initial pH value, the calcination at 975°C resulting in several times smaller crystalline sizes than the calcination at 1050°C. In Table 4 are shown the final refined parameters for samples made from the pH=7.5 solution and calcined at 975°C and 1050°C.

Table 4. The values for parameters from the Rietveld refinements of the samples made from the pH = 7.5 solution and calcined either at 975 or 1050°C. The standard deviations of the last numbers are shown in the parenthesis. A sample calcined at 975°C is fitted with a monoclinic P $2_1/n$ structure, a sample calcined at 1050°C with a tetragonal I4/m structure. [**P2**]

Sample (pH=7.5)	975°C	1050°C
χ^2	1.72	2.47
Average size (nm)	31.03(4)	197(10)
a (Å)	5.5793(8)	5.57212(8)
b (Å)	5.5750(6)	5.57212(8)
c (Å)	7.9290(5)	7.9053(2)
β(°)	90.366(5)	90
Ordering (%)	90	85
$SrMoO_4$(wg%)	8	3

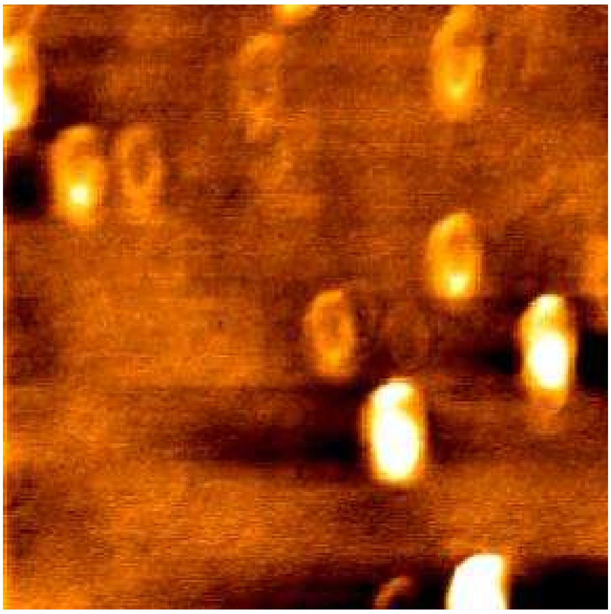

Figure 12. AFM image of the SFMO particles. The image size is 1x1 μm^2 and the height of the particles 2 nm.

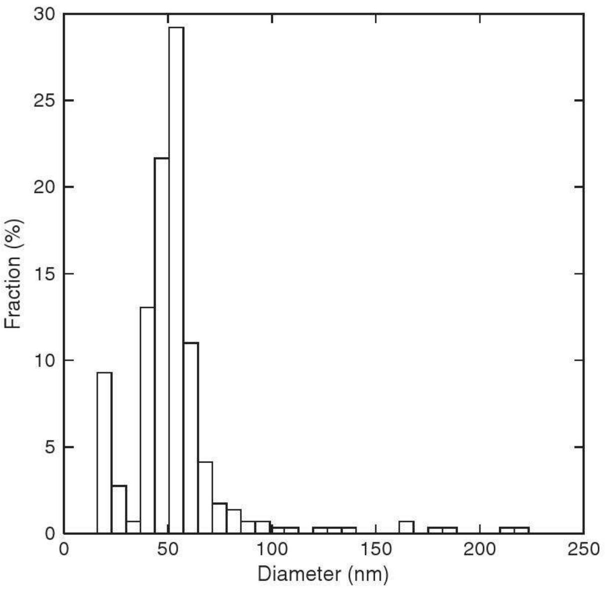

Figure 13. Particle size distribution from 290 particles measured with AFM from the smallest single particles on the sample made from the pH = 7.5 solution and calcined at 975° [**P1**].

3.1.2 AFM

For AFM measurements, a small amount of SFMO powder and ethanol were mixed and kept in an ultrasonic bath for half an hour to get all the possible agglomerations broken. A small amount of the ethanol/SFMO mixture was pipeted on an ultrasonic homogenizator tip which sprayed it on a polished Si wafer. The Si wafer was imaged with the AFM and the images were analyzed to obtain the size distribution of the crystallites.

In all the images, particles were disk shaped and clearly separated from their neighbouring particles indicating that the sizes obtained from the analyzation are the sizes of single particles (Fig. 12). The obtained height distribution gave an average height of 5 nm. This does not agree with the size obtained from the XRD refinement and is also too small when considering the quite high preparation temperatures (975°C). It is possible that the ultrasonic homogenizator gives such a large kinetic energy to the particles that they break on collision on the Si surface. By calculating the particle volumes from the AFM images and then calculating an equivalent sphere diameter, the particle diameter was obtained.

[**P1**]

The obtained diameter distribution is shown in Fig. 13. The mode of the distribution is just over 50 nm which agrees well with the XRD result.

3.2 Magnetic properties of the powders

3.2.1 Magnetization measurements

Magnetic measurements were made with a SQUID magnetometer. The measured samples were chosen based on the XRD measurements. Chosen samples were the ones calcined at 975 and 1050°C, labeled A and B, respectively, and were made from the starting solution with the highest used pH values of 7.5 and 9.0, labeled 5 and 6, respectively.

In Figure 14 are shown the magnetization loops at 5 K and 300 K in an applied field of -4 to 4 T. As can be seen, the A set of samples has notably lower magnetization values than B set. Figure 15 confirms that the magnetic behavior of the A and B samples is completely different. In this temperature dependence measurement made on the sample set with the pH=7.5 starting solution, the B sample shows a normal ferromagnetic transition at ≈ 415 K, while sample A magnetization grows almost linearly without any clear transition.

According to the XRD measurements, there was not much difference in the purity or antisite ordering between these samples. Thus the difference in magnetization values is related to the crystalline size difference of these sample sets. The B samples ($D > 100$ nm) magnetization values were as expected based on the antisite ordering and taking account the itinerant electrons. The A samples ($D < 100$ nm) have remarkably low magnetization values, which can not be explained by such means.

To find an explanation to the peculiar magnetic behavior of the sample A, zero field cooled (ZFC) and field cooled (FC) magnetizations were measured from 110 to 3.5 K at 1 mT field (Fig. 16). Superparamagnetism causes a maximum in the ZFC curve. At temperatures above that maximum, the sample is in a paramagnetic state because the thermal exitations are stronger than the external field, below the maximum the sample is in a ferromagnetic state due to the weakening of the thermal energy. The temperature where the maximum appears is called the blocking temperature, T_{B}, the value of which is dependent on the timescale of the measurement. If the thermal equilibrium is not reached within the measurement timescale, the sample is said to be in a blocked state. The

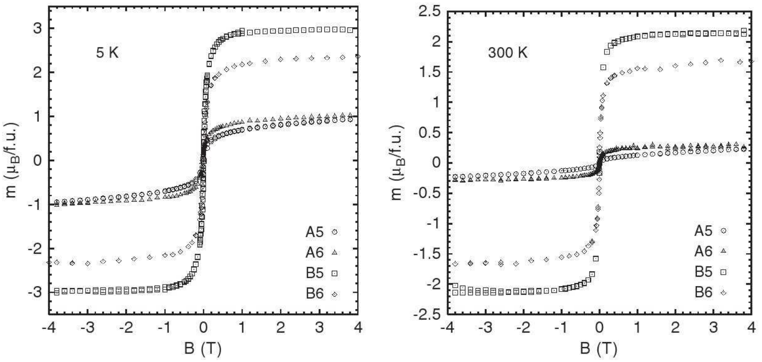

Figure 14. Magnetization measurements at 5 and 300 K for samples calcined at 975 (A) and 1050°C (B). The numbers 5 and 6 refer to the starting solution pH values of 7.5 and 9.0, respectively. [**P1**]

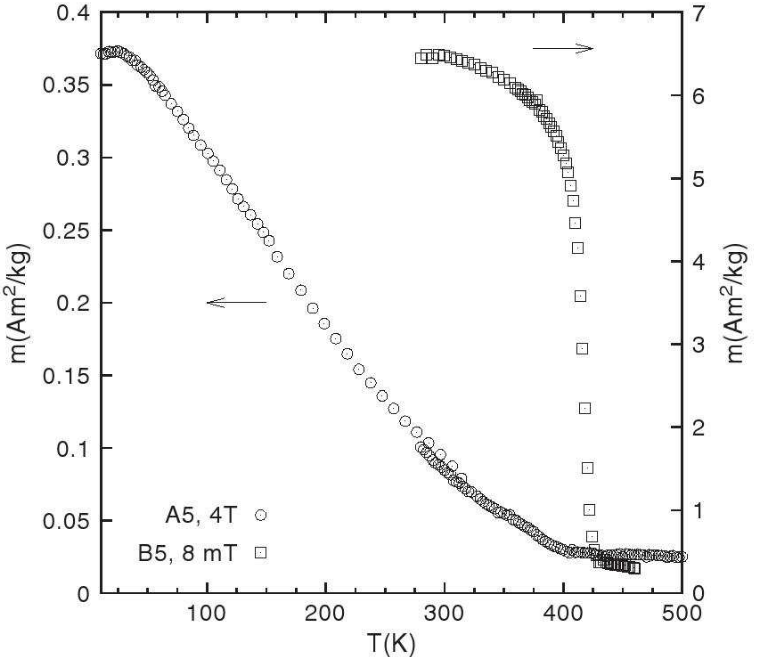

Figure 15. Temperature dependence of magnetization for both samples from 280 K to 460 K in 8 mT. Sample B shows a normal ferromagnetic transition at $T_c \approx$ 415 K. Such a transition is not observable for sample A. Measurements were made on sample set 5. [**P1**]

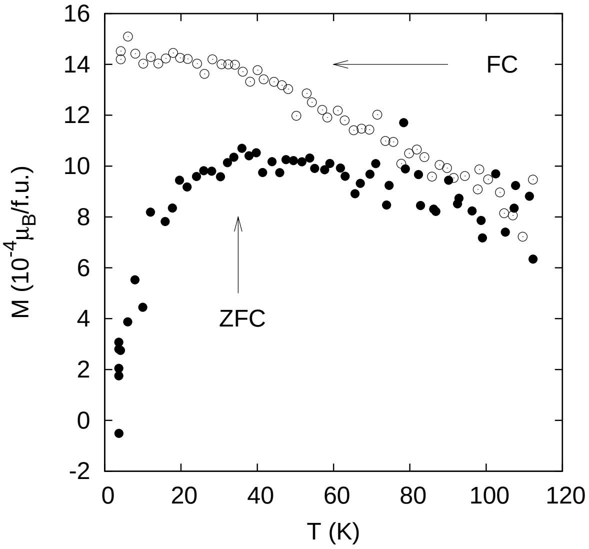

Figure 16. Zero field (solid circles) cooled and field cooled (circles) magnetizations from 110 K to 3.5 K for sample A at 1 mT field. From the ZFC curve it is possible to determine the blocking temperature, T_B, to be 35 K. Below T_B the sample behaves ferromagnetically and above the T_B it is paramagnetic.[**P2**]

SQUID magnetometer is a slow method, τ_SQUID =100–500 s, thus the magnetic moments have plenty of time to reach a thermal equilibrium. When the magnetic moments of the sample are in thermal equilibrium, the sample is in a superparamagnetic state. In Figure 16 a maximum is seen in the zfc-curve around 35 K, which is the T_B for sample A in SQUID measurements.

If the sample really is superparamagnetic, its magnetization should follow the Langevin equation[109–111]

$$M(H,T) = N\mu \left[\coth \frac{\mu H}{k_\mathrm{B}T} - \frac{k_\mathrm{B}T}{\mu H}\right], \tag{1}$$

where N is the number of particles, μ is the magnetic moment per particle, T is the temperature, H is magnetic field and k_B stands for the Boltzmann constant. Figure 17 shows the fit of the Langevin equation with the measured magnetization of the sample, where the contribution of metallic iron is substracted from the measured signal.

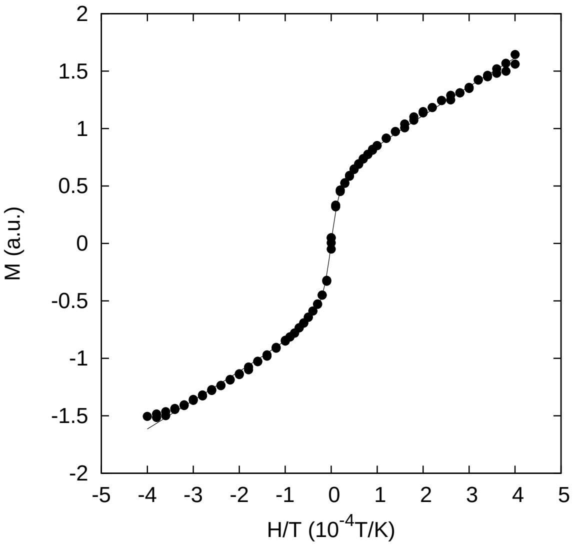

Figure 17. Magnetization vs. applied field divided by temperature. Measurement was made for sample A in a constant temperature of 300 K ($> T_\mathrm{B}$) from -4 T to 4 T. Experimental data, from which the Fe impurity contribution was subtracted, is presented with dots, while the curve was obtained from a fit using the Langevin equation. [**P2**]

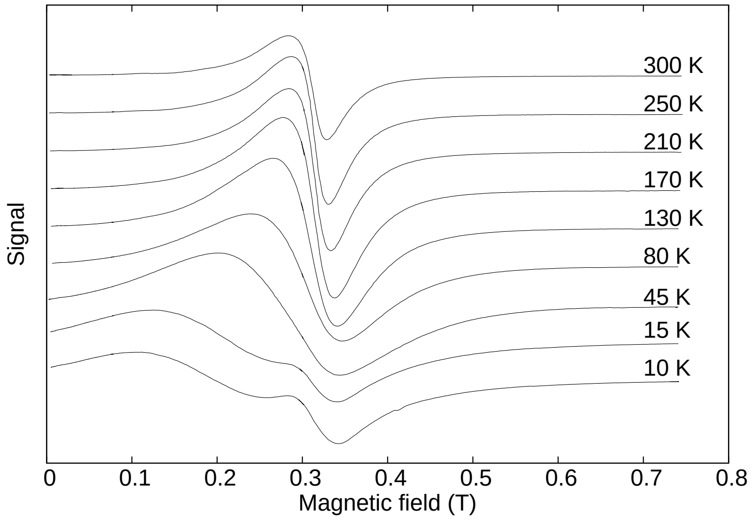

Figure 18. FMR measurements for a sample calcined at 975°C, crystalline size 31 nm. The signal is paramagnetic although the temperature is much lower than T_c. At temperatures below 45 K, the signal changes to be ferromagnetic. [**P2**]

3.2.2 FMR and Mössbauer spectrometry

Ferromagnetic resonance measurements were made on the two SFMO powder samples with particle sizes of 31 and 197 nm. Temperature ranged from 10 to 300 K and fields from 0 to 0.75 T. Powder samples are randomly oriented, thus directional dependence broadens the measured peaks on both samples (Fig. 18 and 19). As the temperature decreases, the anisotropy field direction dependence increases.

Figure 18 shows the measurements on the 31 nm sample. The signal is paramagnetic above 45 K and a peak shift is observed towards lower fields when the thermal excitations get weaker. The signal for the 197 nm sample is ferromagnetic at all temperatures (Figure 19), although a similar peak shift is observed. At low temperatures a free electron peak can be resolved which could be caused by the surface layer of the particles or extremely small particles in the samples. For the 31 nm sample the blocking temperature, T_B, is observed from paramagnetic to ferromagnetic change in the signal shape. At FMR timescale, 10^{-10}–10^{-9} s, $T_{B,FMR} \approx 45$ K.

In Figure 20 are shown the Mössbauer spectrometry measurements at 77 K

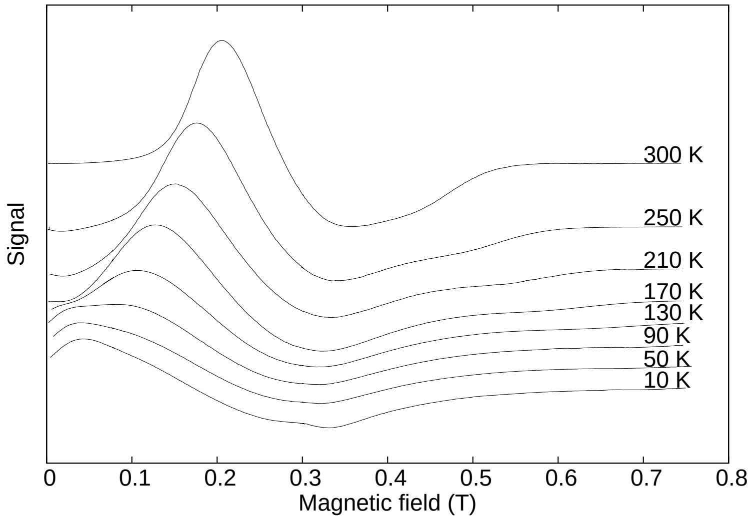

Figure 19. FMR measurements for a sample calcined at 1050°C, crystalline size 197 nm. The observed signal is ferromagnetic throughout the whole temperature range. [**P2**]

(made by J. Lindén at Åbo Akademi). The results indicate that roughly 30 % of the sample A grains exceed the sizelimit required for superparamagnetism (lower spectrum in Fig. 20). The timescale for these measurements is 141 ns, which is the life time of an excited ^{57}Fe -state. Below the blocking temperature the superparamagnetic grains can be stabilized, but above T_B the signal is paramagnetic. Sample B has a typical SFMO spectrum (upper spectrum in Fig. 20) and from it could be confirmed the AS-order of the samples obtained from the Rietveld refinement. The internal fields of Fe atoms depend on the neighboring atoms, these fields can be identified with Mössbauer measurements and therefore the AS order can be obtained.

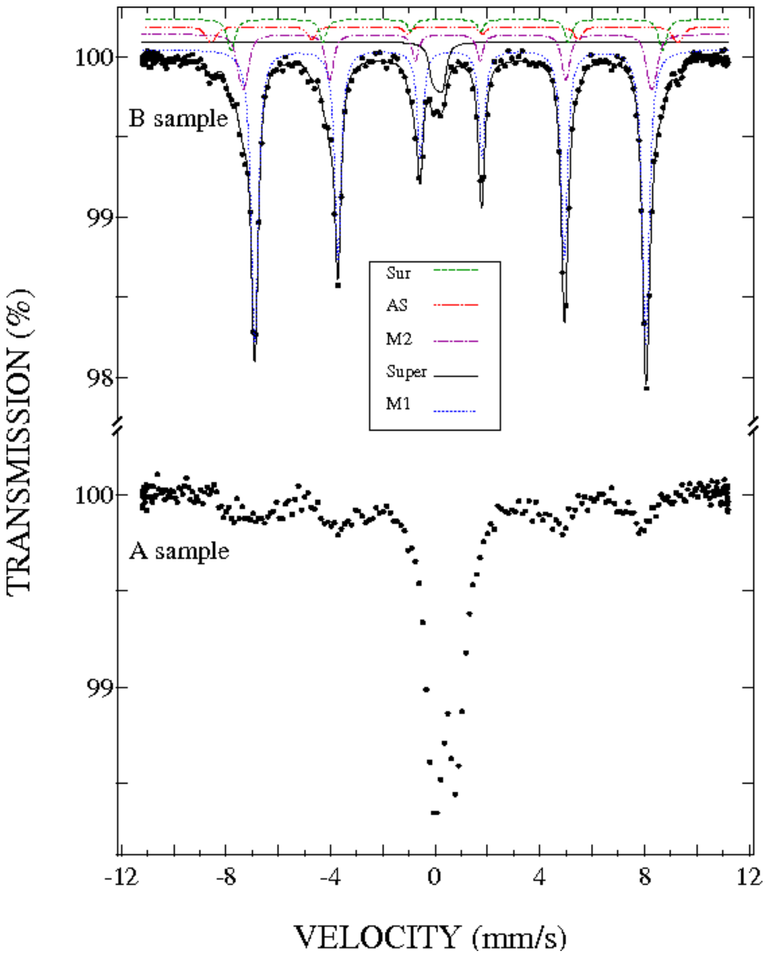

Figure 20. Mössbauer measurement spectra for both samples, measured at 77 K. Upper spectrum, sample B, shows typical SFMO Mössbauer spectra whereas sample A, lower spectrum, has broadened paramagnetic doublet and weak magnetic wings. [**P2**]

4 Physical properties of the thin films deposited from target made by the citrate-gel method

4.1 Structure of the films

4.1.1 X-ray diffraction

The target was made from the nanosized SFMO powder. The powder was pressed into a pellet and then heat treated three times at 975°C. The untexturized final target was measured with XRD (Fig. 21). No detectable peaks of impurities were observed. Figure 21 shows the Rieveld refinement made with a single phase of SFMO. Refinement gave the lattice parameter values $a = b = 5.56$ Å, $c = 7.89$ Å and an average grainsize of 100 nm. The lattice parameters are slightly compressed in comparison to the powder diffraction values due to the pellet form of the sample. The Fe-Mo occupancies an gives antisite ordering of 77 % and the refinement χ^2 a value of 1.61.

The ablation temperature affects the film appearance. Films prepared at 780-790°C were brown, and some yellowish impurity was observed. Red coloured films were Fe rich, prepared at temperatures of 800 – 850°C. An ablation temperature of 860°C resulted in a shiny blueish black film of SFMO. The quality of these films was further improved by in-situ post-deposition annealing a 880°C. The XRD 2θ scan of the film ablated at 860°C shows the SFMO $(00l)$ peaks (Fig. 22) as expected for thin films. Besides SFMO, no other phase peaks were observable.

4.1.2 Texture measurements

For the thin film texturization, the measured SFMO peak needs to be carefully chosen to avoid overlapping with the dominant substrate peaks. Texture was measured on a SFMO (204) peak at $2\theta = 57.106°$. In Fig. 27 is shown the measurement made on the SFMO peaks, which shows a clear c-axis orientation. Other peaks besides (204) and (024) (inner peaks) are the peaks of (132) and (312). Similar measurements were made on the Fe (110) peak ($2\theta = 44.68°$) and $SrMoO_4$ (112) ($2\theta = 27.68°$), but no trace of these impurities were found (Fig. 24); they were not detected in the 2θ scans either (Fig. 22).

Films grew equally well on both substrate materials, STO and MgO. The SFMO lattice $a - b$ axes plane is turned 45° on both substrates in comparison to the subtrate $a - b$ plane, similarly as for LCMO films shown in Fig. 8. STO causes

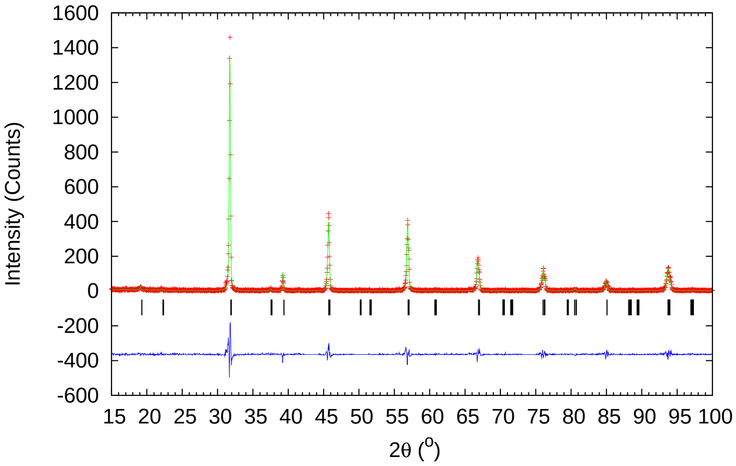

Figure 21. XRD measurement (crosses) and Rietveld refinement (line) for three times at 975 °C heat treated target. The refined phase is SFMO and χ^2 is 1.61.[**P3**]

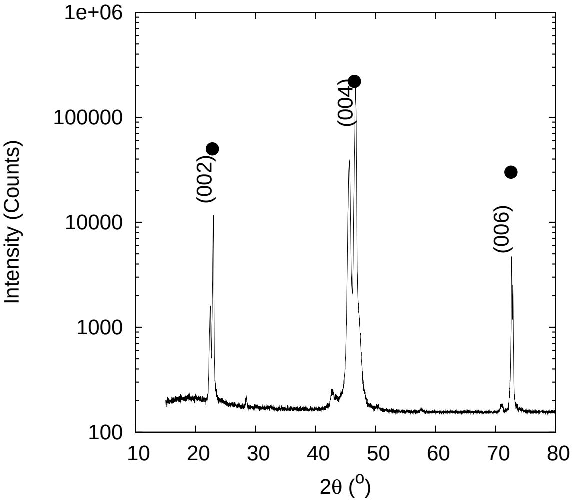

Figure 22. XRD measurement on the film ablated at 860°C on STO. SFMO (00*l*) and substrate peaks (solid circles) are seen.[**P3**]

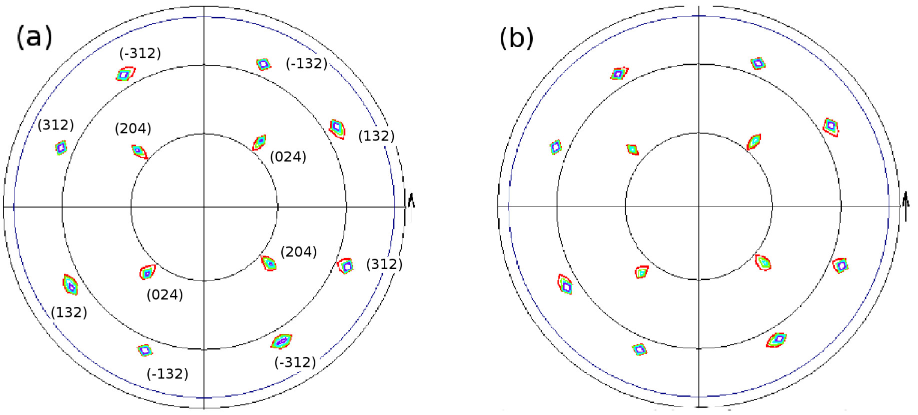

Figure 23. Film texture measurements on films grown on both subtrates at 860°C, STO (a) and MgO (b). Measurement was taken over the SFMO (204) peak at $2\theta = 57.106°$. The peak was chosen to avoid the substrate peaks. The texture measurement shows full texturation. [**P3**]

a little compression of the SFMO lattice, but neither of the substrates cause so much strain or compression that it would disturb the film lattice parameters or the position of the peaks, as can be concluded from the pole figures. Because the SFMO films are so thin, the antisite ordering can not be defined with XRD as the substrate peaks are too dominant.

Figure 25 is made on the film grown on MgO below 860°C. The measurement emphasizes the difference between pure and well texturized films and films with low texturization and impurity phases. The measured peaks are the same as in Figs. 27 and 24. SFMO is poorly texturized whereas impurity phases are present and show partial texturation. This is due to the lower ablation temperature, as that was the only changed ablation parameter between these sets of measurements. The impurity phases were also clearly observable on 2θ scans as well as in the color changes of the films.

4.1.3 AFM, SEM

Characterization of the film surface was made with AFM and SEM (Fig. 26). An edge was etched with H_3PO_4 on the film and the thickness of the film was measured with AFM scanning across the edge. The usual thickness for the ablated films was approximately 100 nm. AFM measurements gave the surface

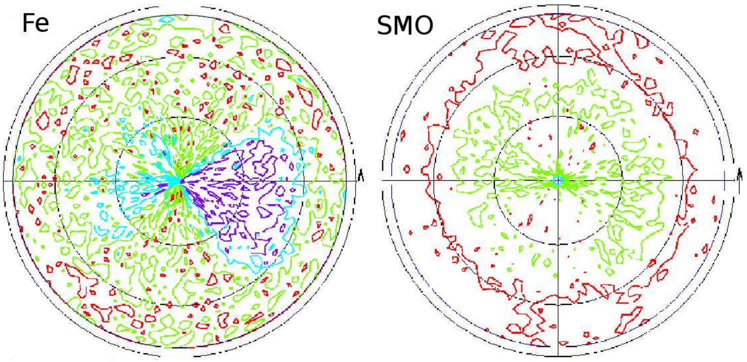

Figure 24. The texture measurements on possible impurities in the film grown on STO at 860°C were measured over the Fe peak at $2\theta = 44.68^\circ$ and at $SrMoO_4$ $2\theta = 27.68^\circ$. No indication of impurity phases is seen in either of the pole figures. [**P3**]

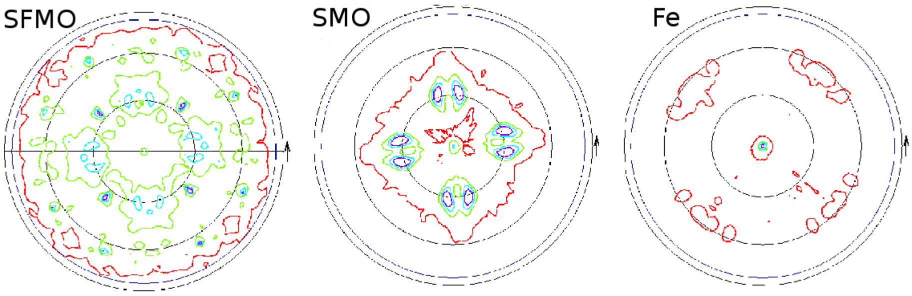

Figure 25. The texture measurements of the film made on MgO at too low temperature. SFMO is not completely oriented, Fe shows clear peaks and some texturization as does SMO. 2θ values are the same as used in Figs. 27 and 24.[**P3**]

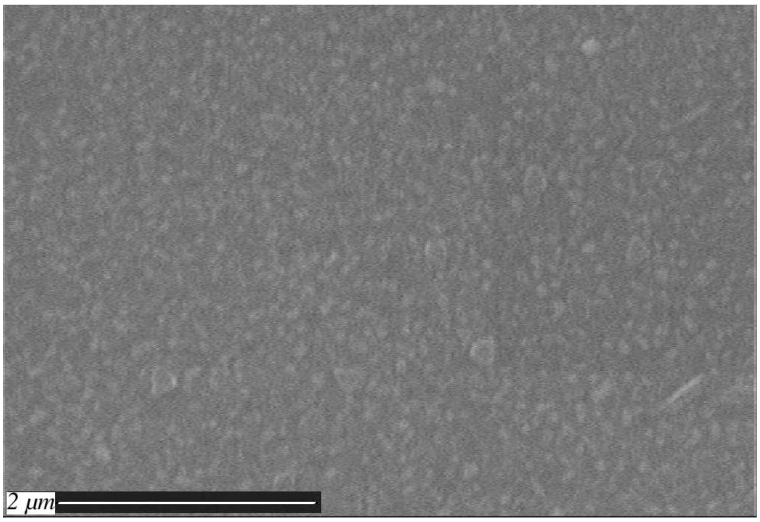

Figure 26. SEM image of the film surface showing a homogenous surface structure with small, evenly distributed particulates. [**P3**]

RMS roughness value of 5.3 nm for the 100 nm thick film on STO, and the SEM images show a homogenous structure for the same film.

4.2 Magnetic measurements

Magnetic measurements for the good films were made with a SQUID magnetometer at 5 and 300 K between -2 and 2 T fields. At both temperatures the magnetization values were nearly the same, thus the Curie temperature should lie above the room temperature.

5 Photomagnetism in LCMO films

The influence of vacuum and O_2 annealing on the structural and magnetic properties of LCMO films with $x = 0.1$ is investigated. In addition, the effect of illumination on O_2-treated and vacuum treated films is studied in order to understand the role of oxygen vacancies in forming the persistent photoinduced magnetization (PPM) state. The parameters used for the heat treatments are listed in Table 5.

5.1 X-ray diffraction

XRD analysis revealed no impurity phases and showed full texturing (Fig. 27). The c-axis was perpendicular to the film surface as is the case for SFMO films. Lattice parameters are given in Table 6. In comparison to the bulk values, $a = 0.548$ nm, $b = 0.551$ nm and $c = 0.778$ nm [112], strain is observed in the films.

As shown in Table 6, thermal annealing in oxygen contracts the unit cells due to the oxygen absorption to the sample (sample B), whereas annealing into vacuum expands the unit cell due to oxygen removal from the lattice. This intuitionally opposite result is explained by the Mn–ion valence change, since the cation–cation bond is larger (oxygen removal) than the cation–oxygen–cation bond (oxygen absorption) [113]. Perovskite manganites have a stable structure in the oxygen stoichiometric phase [114]. The change of lattice parameters is related to the ionic radii of Mn^{3+} and Mn^{4+}, 0.07 nm and 0.05 nm, respectively and oxygen 0.12 nm. The lattice parameter changes caused by the changes in the Mn^{4+}/Mn^{3+} ratio are more dominant than the changes between oxygen absorption or removal, thus the lattice parameters decrease with increasing O_2 content, and release of oxygen from the structure increases the size of the unit cell.

Heat treatments widen the diffraction peaks (Table 6, Figure 27) due to the changes in the unit cells. Especially the vacuum treatment changes the peak shape (Figure 27(D)). Diffraction peaks widen due to the lattice strain and changes in the unit cell volume.

5.2 AFM

Atomic force microscopy images of the LCMO films are shown in Figure 28.

The heat treatments have a clear effect on the surface structure of the samples. As-deposited films (Fig. 28(a)) have square-shaped grains oriented along

Table 5. Parameters used in post-annealing treatments of LCMO films on (001) STO substrate. [**P4**]

Sample	Treatment	T (°C)	P (torr)	Annealing time	Heating/ cooling rate
A	as-deposited	780	0.3	-	-
B	O_2	800	flowing O_2	24 h	1°C/min
C	vacuum	700	10^{-2}	15 min	10°C/min
D	vacuum	700	10^{-4}	15 min	10°C/min

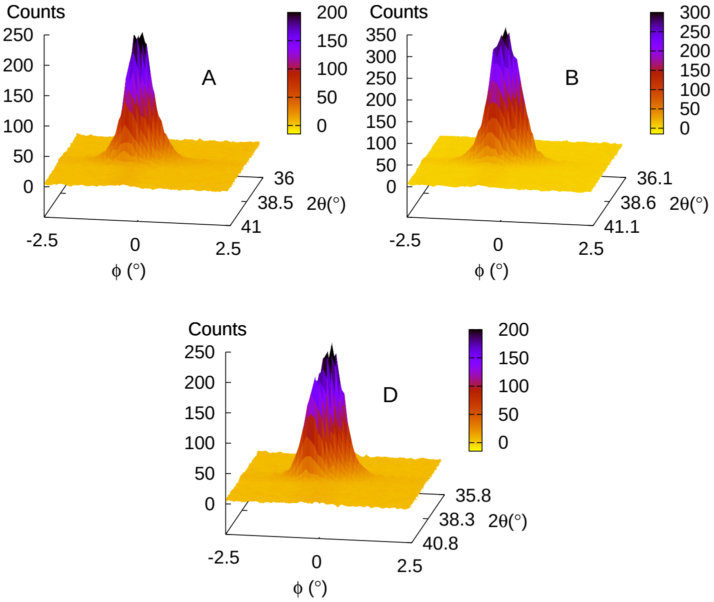

Figure 27. $2\theta-\phi$ scans over the (211) peaks for LCMO films grown on (001) STO substrates: (A) as-deposited, (B) post-annealed in O_2 and (D) in vacuum.[**P4**]

Table 6. The lattice parameters, average peak FWHM widths in 2θ and the difference in unit cell volume (ΔV) as compared to bulk values for the films deposited on (001) STO and after annealings in oxygen (B) at 800°C and in vacuum at 700°C (D).[**P4**]

Sample	a (nm)	b (nm)	c (nm)	FWHM (°)	ΔV (%)
A	0.5477	0.5491	0.7672	0.53	-1.96
B	0.5444	0.5464	0.7691	0.55	-2.78
D	0.5488	0.5499	0.7740	0.63	-0.74

the crystallographic [110]-direction of LCMO, and show quite good connectivity. The average width of the growth islands is about 300 nm and the grain height on the surface is between 2 - 10 nm. Oxygen annealing (Fig. 28(b)) increases the size of the grains, especially their height is increased up to 50 nm and the islands become roundish and randomly oriented. The vacuum treated samples (Fig. 28(c)) have grains of width 100-200 nm which is smaller than in the as-deposited films, while the grain heights are only a couple of nanometres as in the as-deposited films. The basic structure is also smoother, the islands are fused together and are now oriented along the LCMO a/b-axes, having small pores penetrating towards the substrate.

The surface root mean square roughness (RMS roughness) changes strongly, since the as-deposited and vacuum annealed samples are rather smooth, with a RMS roughness of 2.5 and 1.9 nm, respectively. The annealing in oxygen causes the surface roughness to increase to 17.7 nm. This is also observable in Figure 28.

5.3 Magnetic measurements

The $M_{\mathrm{ZFC}}(T)$ and $M_{\mathrm{FC}}(T)$ curves shown in Figure 29 are found to deviate from each other at a temperature that depends on the way of cooling the sample (ZFC or FC in 20 mT field) or whether it was illuminated or not before the measurements. In unilluminated samples A and B, there is a broad maximum in the $M_{\mathrm{ZFC}}(T)$ curves around a freezing temperature, $T_{\mathrm{f}} \approx 45$ K, below which the difference of $M_{\mathrm{FC}}(T) - M_{\mathrm{ZFC}}(T)$ starts to deviate from zero, while $M_{\mathrm{FC}}(T)$ is almost temperature independent.

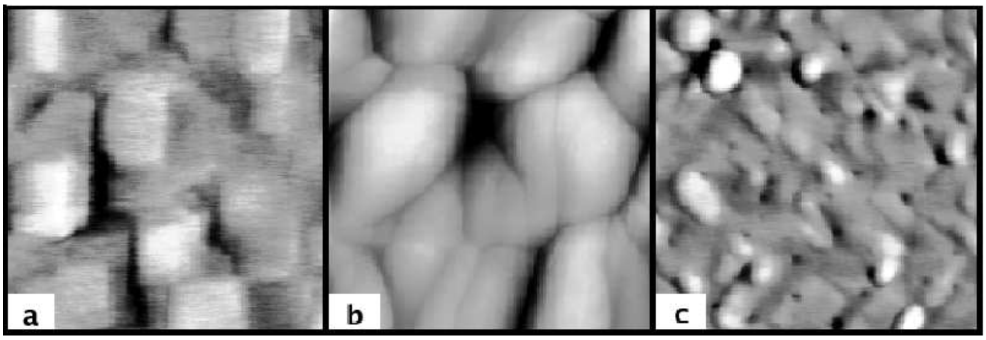

Figure 28. Atomic force microscopy scans of as-deposited (a), O_2 annealed (b) and vacuum annealed (c) LCMO films. The area of the images is 1×1 μm^2 and the grayscales (height from black to white) are 5, 50 and 10 nm for (a), (b) and (c), respectively.[**P4**]

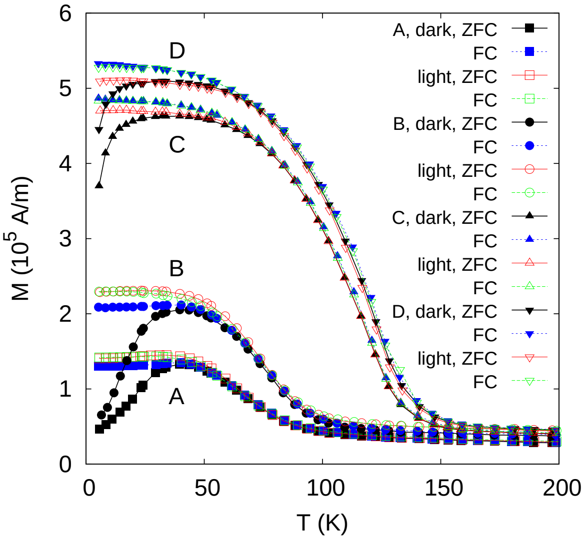

Figure 29. Temperature dependence of M_{ZFC} and M_{FC} (B = 20 mT) measured before and during illumination of the films. The solid symbols refer to measurements in dark and the open symbols to those made under illumination with the 514.5 nm wavelength of the Ar ion laser. [**P4**]

Table 7. Curie temperature, coercive field (B_c) and the ratio of maximum magnetization M_{max} and the remanent magnetization M_{rem} of the films before and during illumination are calculated from the temperature dependence of M and the hysteresis loop curves shown in figures 29, 30 and 31. [**P4**]

	Unilluminated			Illuminated		
Film	T_c(K)	$B_{c,5K}$(mT)	M_{rem}/M_{max}(%)	T_c(K)	$B_{c,5K}$(mT)	M_{rem}/M_{max}(%)
A	89	17	35	89	0	14
B	100	24	42	100	0	17
C	146	8	38	146	3	35
D	152	3	62	152	3	58

Similar enhancements of $M(B)$ and T_C have been observed in oxygen annealed $La_{0.7}Ca_{0.3}MnO_3$ films [98] and in $La_{0.84}Ca_{0.16}MnO_{3-\delta}$ films where these changes were related to the increase of the ratio Mn^{4+}/Mn^{3+} [115].

The virgin $M(B)$ curves, measured at 5 K up to $B = 100$ mT are shown in Figure 30. Although the as-deposited and the oxygen treated films show practically linear field dependence without illumination, vacuum annealings result in FM type virgin curves. The linear initial magnetization curve $M(B)$ presented for films A and B in Figure 30 in dark and the slight upturn seen after illumination can be attributed to competition between AFM and FM domains [116]. After the first vacuum treatment (film C), the magnetization is not yet saturated at $B = 100$ mT. The second vacuum treatment (film D) leads to steeper increase of the $M(B)$ curve than is observed in the as-deposited and oxygen treated films, and the magnetization is nearly saturated around $B = 100$ mT. Because any impurity phases were not found in these films and according to surface analysis shown in Figure 28 there is a clear difference in the size of the grains, the differences between the samples could be explain by the magnetic domain size and by the size and movements of domain walls in similar oxides [117].

In Figure 31 are shown the magnetic hysteresis loops measured at 5 K between -100 mT and 100 mT for the films (A - D). The oxygen annealed film (B) has the most open loop, in terms of the coersivity field B_c, and annealing in vacuum (C - D) shrinks and sharpens the loop. After the first vacuum treatment (C),

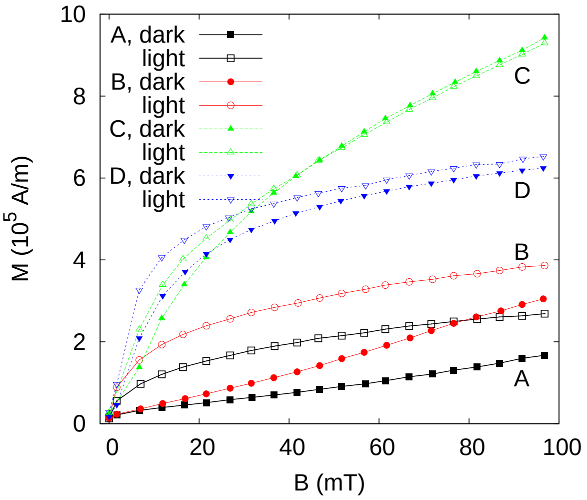

Figure 30. Virgin magnetization curves observed at 5 K for all the films before (solid symbols) and during (open symbols) illumination. [**P4**]

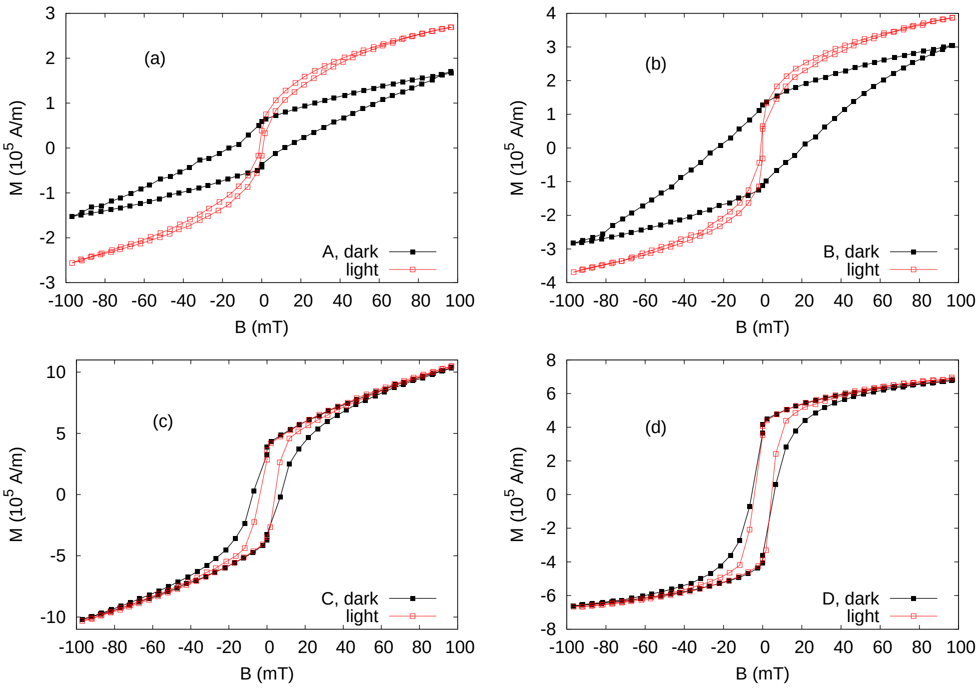

Figure 31. The hysteris loops measured at 5 K between -100 and 100 mT on as-deposited, oxygen annealed and vacuum annealed films (C and D) and (d) before (solid symbols) and during (open symbols) illumination. [**P4**]

the magnetization is not saturated in the low field region, as observed after the second vacuum treatment (D). In as-deposited and oxygen treated films A and B the hysteresis loops can be closed completely by illumination, but the vacuum annealed films are much less influenced.

The values of B_c and the ratio of M_{rem}/M_{max}(100 mT) are shown in Table 7. It is noteworthy that when the FM component has been increased by vacuum annealing, the photoinduced effect is much smaller or even lacking (D), because the maximum ferromagnetism has already been reached by an optimum $\mathrm{Mn}^{4+}/\mathrm{Mn}^{3+}$ ratio induced in the vacuum treatment [115].

As shown in Figures 27 and 30, the corresponding changes are seen also in the XRD and in virgin curve measurements. Large surface roughness of O_2-annealed films indicates the presence of more defects in the films that may act as magnetic pinning sites and therefore increase the coercive field [118]. This is in accordance with the atomic force microscopy results showing that the oxygen treated films have the largest surface roughness and highest B_c without illumination (Table 7, Figure 31 (c)-(d)).

5.4 Photoinduced persistent magnetization

Persistent photoinduced magnetization (PPM) growth and relaxation can be described by a streched exponential law, the Kohlrausch expression,

$$M_\mathrm{ill}(t) = M_\mathrm{ill}^{sat}\exp[-(t/\tau)^{\beta}], \tag{2}$$

where $\tau(T, B)$ is a characteristic time and the exponent β is dispersion parameter $0 < \beta < 1$. The exponents β_g and β_r (indices g growth and r relaxation) in equation (2) are related to growth and relaxation of the PPM, respectively. In Figure 32 are shown the growth and relaxation of the PPM state, the solid line showing the fitted Kohlrausch expression. For relaxation of M_ill in film A, the value of $\beta_r = 0.3$ and for the vacuum annealed film D $\beta_r = 0.29$ are nearly the same. A difference occurs at the development of the PPM state, for sample A $\beta_g = 0.43$, whereas for sample D the value is considerably lower, $\beta_g = 0.18$.

The predicted value for β_g to describe a charge transfer process induced by phonons in the presence of randomly distributed traps is 3/7 [119]. The value of β_g for sample A is close to that 3/7 value. In the vacuum treated, oxygen deficient sample D, the PPM is nearly completely missing, thus relating the phenomena on the oxygen atoms in the LCMO structure.

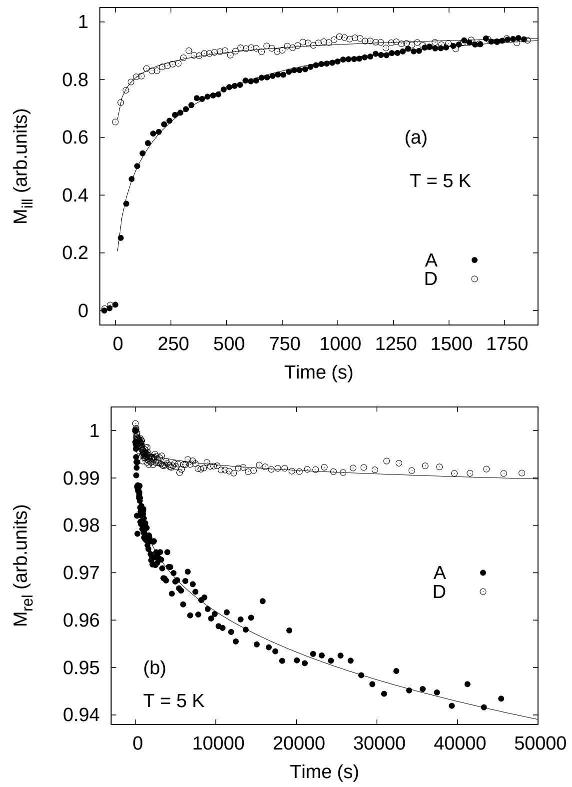

Figure 32. Time dependence of the growth of photoinduced magnetization, M_{ill}, at 5 K and $B = 20$ mT for as-deposited (A) and vacuum annealed (D) LCMO films (a) and relaxation of the PPM state (b). The solid lines show fits with the stretched exponential law (2).

The time dependence of PPM observed in LCMO resembles the photoinduced superconductivity in oxygen-deficient $\mathrm{YBa_2Cu_3O}_x$ films [101, 120]. In those films the photoexcited electrons are believed to be trapped at oxygen vacancies in the superconducting $\mathrm{CuO_2}$ planes [121].

6 Conclusions

An improved method for the preparation of SFMO nanopowder is introduced. The applicability of the nanopowder for preparation of PLD targets and SFMO thin films is investigated. Structural and magnetic properties of the powders were studied with several methods.

The citrate-gel method was optimized by preparing several sets of powders with varying pH values from 1.5 to 9.0 in the starting solution. It was observed that SFMO formed already at 500°C, but the formation was very much pH dependent. Only the lowest pH values (1.5 and 3.0) resulted in SFMO formation at this temperature. Several impurity phases were also present in these samples. The ordering of the SFMO was also pH dependent, and 80% ordering was obtained with the highest pH values.

At higher calcination temperatures more SFMO was formed. The powder crystalline size was dependent on the calcination temperature, the smallest average size being 32 nm. These powders were calcined at 975°C and had strongly reduced values for magnetization, whereas powders calcined at 1050°C and over 100 nm size had the expected magnetic properties.

Further magnetization measurements showed clear differences in the samples caused by the difference in the crystalline sizes. The 197-nm crystallites of SFMO behaved as ordinary bulk material, whereas the 31-nm crystallites did not. According to the results obtained by the SQUID magnetometer, FMR and Mössbauer spectroscopies, the 31-nm sized SFMO behaved superparamagnetically having a blocking temperature of $T_{\mathrm{B,SQUID}} = 35$ K. Thus, the superparamagnetic limit in SFMO crystalline size had been found to be somewhere between 31 nm and 197 nm, and for applications the minimum size for SFMO particles retaining their ferromagnetic properties seems to be approximately 50 nm.

SFMO thin films were made by pulsed laser deposition from a self made nanotarget. The target was made with the above mentioned citrate-gel method and was pure, well ordered SFMO, which resulted in pure, fully texturized SFMO films.

The ablation parameters were optimized and the importance of the right substrate temperature has been illustrated with XRD measurements between the good and bad films. The XRD measurements showed that the SFMO films prepared with right parameters were fully c-axis oriented and without impurity phases, AFM and SEM images showing that the film surface was smooth and homogenous. Magnetization measurements show similar magnetization values at low and high temperatures, thus showing the Curie temperature to be substantially higher than room temperature.

The structural and magnetic properties of $La_{0.9}Ca_{0.1}MnO_3$ films were investigated before and after post-deposition thermal annealings in an oxygen atmosphere or in vacuum. Compared with the as-deposited films, increasing of the oxygen content by thermal annealing practically doubles the magnetization of the films. Even much stronger increase of the magnetization can be obtained by annealing the films in vacuum. This is related to the oxygen reduction in the lattice and the vacancies which are formed. Single electrons can be trapped in these vacancies and with the neighboring moments these electrons form self trapped magnetic polarons, thus increasing the magnetization.

Persistent photoinduced magnetization, excited by green light, is observed in the as-deposited and in oxygen annealed LCMO films in external magnetic field, but in vacuum annealed film the effect is weak or completely missing. This observation relates the photoinduced magnetization to the non-bonding oxygen 2p hole with a wide orbit and ferromagnetic interaction with the Mn 3d shell. In this spectral region strong dipole-allowed O 2p – Mn 3d charge transfer transitions occur. The ground state of this excitation is a high-spin Mn^{2+} state.

With the post-deposition treatments and the observed photoinduced magnetization, the important role of oxygen vacancies in the magnetic properties of low-doped LCMO is clarified.

References

[1] M. Julliere, Phys. Lett. A **54**, 225 (1975).

[2] M. N. Baibich, Phys. Rev. Lett. **61**, 2472 (1988).

[3] G. Binash, Phys. Rev. B **39**, 4828 (1988).

[4] S. Jin *et al.*, Appl. Phys. Lett. **54**, 584 (1988).

[5] H. A. Kramers, Physica **1**, 182 (1932).

[6] C. Zener, Phys. Rev. **82**, 403 (1951).

[7] A.-M. Haghiri-Gosnet and J.-P. Renard, J. Phys. D.:Appl. Phys. **36**, R127 (2003).

[8] S. Nakayama, T. Nakagawa, and S. Nomura, J. Phys. Soc. Japan **24**, 219 (1968).

[9] K.-I. Kobayashi *et al.*, Nature **395**, 677 (1998).

[10] T.-T. Fang and T.-F. Ko, Journal of the American Ceramical Society **86**, 1453 (2003).

[11] J. Navarro *et al.*, Materials Research Bulletin **38**, 1477 (2003).

[12] M. T. Anderson, K. B. Greenwood, and G. A. Taylor, Prog. Solid St. Chem. **22**, 197 (1993).

[13] J. Rager, M. Zipperle, A. Sharma, and J. L. MacManus-Driscoll, J. Am. Ceram. Soc. **87**, 1330 (2004).

[14] A. S. Ogale, S. B. Ogale, R. Ramesh, and T. Venkatesan, Appl. Phys. Lett. **75**, 537 (1999).

[15] L. Balcells *et al.*, Appl. Phys. Lett. **78**, 781 (2001).

[16] M. Garcia-Hernandez *et al.*, Phys. Rev. Lett. **86**, 2443 (2001).

[17] D. Sanchez *et al.*, Phys. Rev. B **65**, 104426 (2002).

[18] D. Sarma *et al.*, Solid State Communications **114**, 465 (2000).

[19] B. J. Park *et al.*, J. Magn. and Magn. Mater. **272-276**, 1851 (2004).

[20] X. Z. Liao *et al.*, J. Appl. Phys. **96**, 7747 (2004).

[21] T. Shimada *et al.*, Chem. Mater. **15**, 4494 (2003).

[22] P. M. Woodward, Acta Crystallogr., Sect.B: Struct. Sci. **53**, 32 (1997).

[23] J. Navarro *et al.*, J. Phys. Cond. Mat. **13**, 8481 (2001).

[24] L. Balcells *et al.*, Appl. Phys. Lett. **78**, 781 (2001).

[25] G. Liu *et al.*, J. Phys. Cond. Mat. **15**, 2053 (2003).

[26] G. Liu *et al.*, Journal of Alloys and Compounds **353**, 42 (2003).

[27] P. Battle, T. Gibb, C. Jones, and F. Studer, Journal of Solid State Chemistry **78**, 281 (1989).

[28] J. B. Goodenough and R. I. Dass, Int. J. Inorg. Mater **2**, 3 (2000).

[29] J. Lindén *et al.*, Phys. Rev. B **68**, 174415 (2003).

[30] J. Navarro *et al.*, Phys. Rev. B **70**, 054423 (2004).

[31] J. Lindén, T. Yamamoto, M. Karppinen, and H. Yamauchi, Appl. Phys. Lett. **76**, 2925 (2000).

[32] T.-Y. Cai and Z.-Y. Li, J. Phys. Cond. Mat. **16**, 3737 (2004).

[33] Y. H. Huang, J. Lindén, H. Yamauchi, and M. Karppinen, Chem. Mater **16**, 4337 (2004).

[34] D. Sanchez *et al.*, J. Phys. Cond. Mat. **17**, 3673 (2005).

[35] W. Prellier *et al.*, J. Phys. Cond. Mat. **12**, 965 (2000).

[36] J. Alonso *et al.*, Chem. Mater. **12**, 161 (2000).

[37] J. Alonso *et al.*, Chem. Mater. **12**, 161 (1999).

[38] L. S. Lobanovskii, I. O. Troyanchuk, N. V. Pushkarev, and G. Szymczak, Phys. Solid State **43**, 677 (2001).

[39] R. Dass and J. Goodenough, Phys. Rev. B **63**, 064417 (2001).

[40] Y. Moritomo *et al.*, Phys. Rev. B **62**, 14224 (2000).

[41] J. M. Dai *et al.*, Materials Science and Engineering **B83**, 217 (2001).

[42] J. M. Greneche, M. Venkatesan, R. Suryanarayanan, and J. M. D. Coey, Phys. Rev. B **63**, 174403 (2001).

[43] H. Wu, Phys. Rev. B **64**, 125126 (2001).

[44] J. Navarro *et al.*, Phys. Rev. B **64**, 092411 (2001).

[45] J. H. Jung *et al.*, Phys. Rev. B **66**, 104415 (2002).

[46] J. B. Shi *et al.*, Physica B **329-333**, 805 (2003).

[47] J. Shi *et al.*, Applied physics A **78**, 411 (2004).

[48] Q. Zhang *et al.*, Solid State Communications **133**, 223 (2005).

[49] Y. Sui *et al.*, Appl. Phys. Lett. **85**, 269 (2004).

[50] A. H. Habib, C. V. Tomy, A. K. Nigam, and D. Bahadur, Physica B **362**, 108 (2005).

[51] M. Lü *et al.*, J. Phys. Cond. Mat. **18**, 1601 (2006).

[52] A. H. Habib, A. Saleem, C. V. Tomy, and D. Bahadur, J. Appl. Phys. **97**, 10A906 (2005).

[53] K. Yoshida, S. Kihara, and H. Shimizu, Physica B **359-361**, 1330 (2005).

[54] J. H. Kim, G. Y. Ahn, S.-I. Park, and C. S. Kim, J. Magn. and Magn. Mater. **282**, 295 (2004).

[55] A. Azad *et al.*, Materials Research Bulletin **37**, 1797 (2002).

[56] N. Massa, J. Alonso, M. Martinez-Lope, and M. Casais, Phys. Rev. B **72**, 214303 (2005).

[57] C. Li, Y. Cailei, X. Junmin, and J. Wang, J. Am. Ceram. Soc **89**, 672 (2006).

[58] J. Santiso, A. Figueras, and J. Fraxedas, Surf. Interface Anal. **33**, 676 (2002).

[59] S. R. Shinde *et al.*, J. Appl. Phys. **93**, 1605 (2003).

[60] A. Venimadhav, F. Sher, J. P. Attfield, and M. G. Blamire, J. Magn. and Magn. Mater. **269**, 101 (2004).

[61] D. Sánchez, M. García-Hernández, N. Auth, and G. Jakob, J. Appl. Phys. **96**, 2736 (2004).

[62] A. di Trolio *et al.*, J. Appl. Phys. **100**, 013907 (2006).

[63] C. Li, Y. Cailei, X. Junmin, and J. Wang, J. Am. Ceram. Soc **88**, 2635 (2005).

[64] C. L. Yuan *et al.*, Physica B **334**, 408 (2003).

[65] W. Song *et al.*, J. Appl. Phys. **89**, 7678 (2001).

[66] M. Retuerto *et al.*, Appl. Phys. Lett. **85**, 266 (2004).

[67] Y. H. Huang, J. Lindén, H. Yamauchi, and M. Karppinen, Chem. Mater **16**, 4337 (2004).

[68] Y. H. Huang, J. Lindén, H. Yamauchi, and M. Karppinen, Appl. Phys. Lett. **86**, 072510 (2005).

[69] T.-T. Fang, M. S. Wu, and T.-F. Ko, Journal of Materials Science Letters **20**, 1609 (2001).

[70] S. Sharma *et al.*, Appl. Phys. Lett. **83**, 2384 (2003).

[71] C. L. Yuan *et al.*, Appl. Phys. Lett. **75**, 3853 (1999).

[72] J. Rager *et al.*, Appl. Phys. Lett. **81**, 5003 (2002).

[73] H. Suwaki *et al.*, J. Magn. and Magn. Mater. **295**, 230 (2005).

[74] T. Yamaguchi, H. Suwaki, K. Kikuta, and S. Hirano, Solid State Communications **133**, 71 (2005).

[75] R. Boucher, Journal of Physics and Chemistry of Solids **66**, 1020 (2005).

[76] R. P. Borges *et al.*, Thin Solid Films **429**, 5 (2003).

[77] T. Manako *et al.*, Appl. Phys. Lett. **74**, 2215 (1999).

[78] H. Asano *et al.*, Appl. Phys. Lett. **74**, 3696 (1999).

[79] W. Westerburg, D. Reisinger, and G. Jakob, Phys. Rev. B **62**, R767 (2000).

[80] M. Besse *et al.*, J. Crystal Growth **241**, 448 (2002).

[81] M. Bibes *et al.*, Appl. Phys. Lett. **83**, 2629 (2003).

[82] D.-Y. Kim *et al.*, Appl. Phys. Lett. **84**, 5037 (2004).

[83] J. H. Song, J.-H. Park, and Y. H. Jeong, J. Appl. Phys. **97**, 46105 (2005).

[84] D. Sanchez *et al.*, J. Magn. and Magn. Mater. **294**, e119 (2005).

[85] T. Fix *et al.*, J. Appl. Phys. **97**, 024907 (2005).

[86] T. Fix *et al.*, J. Appl. Phys. **98**, 023712 (2005).

[87] M. Peurla, H. Huhtinen, and P. Paturi, Supercond. Sci. Technol. **18**, 628 (2005).

[88] P. Paturi, M. Peurla, J. Raittila, and N. H. Andersen, Physica C **433**, 123 (2005).

[89] G. Allodi *et al.*, Phys. Rev. Lett. **87**, 127206 (2001).

[90] M. Hennion *et al.*, Phys. Rev. Lett. **81**, 1957 (1998).

[91] G. Papavassiliou *et al.*, Phys. Rev. Lett. **84**, 761 (2000).

[92] R. Laiho *et al.*, Phys. Rev. B **63**, 94405 (2001).

[93] V. Markovich *et al.*, Phys. Rev. B **66**, 094409 (2002).

[94] P. Schiffer, A. P. Ramirez, W. Bao, and S.-W. Cheong, Phys. Rev. Lett. **75**, 3336 (1995).

[95] Y. Tokura, *Colossal Magnetoresistance Oxides* (Gordon and Breach Science, New York , 2000).

[96] Y. S. Du *et al.*, J. Magn. and Magn. Mater. **297**, 88 (2006).

[97] J. R. Sun *et al.*, Appl. Phys. Lett. **76**, 1164 (2000).

[98] T. Li *et al.*, J. Appl. Phys. **98**, 123505 (2005).

[99] H. Huhtinen *et al.*, Phys. Rev. B **62**, 11614 (2000).

[100] H. Huhtinen, R. Laiho, and V. Zakhvalinskii, Phys. Rev. B **71**, 132404 (2005).

[101] V. I. Kudinov *et al.*, Phys. Rev. B **47**, 9017 (1993).

[102] J. F. Lawler, J. G. Lunney, and J. M. D. Coey, Appl. Phys. Lett. **65**, 3017 (1994).

[103] H. Huhtinen *et al.*, J. Magn. and Magn. Mater. **320**, 1747 (2008).

[104] L. G. Schulz, J. Appl. Phys. **20**, 1033 (1949).

[105] J. Rodriguez-Carvajal, Abstracts of the Satellite Meeting on Powder Diffraction of the XV Congress of the IUCr 127 (1990).

[106] P. Thompson, D. Cox, and J. Hastings, J. Appl. Cryst. **20**, 79 (1987).

[107] O. Chmaissem *et al.*, Phys. Rev. B **62**, 14197 (2000).

[108] R. Kromann *et al.*, J. Appl. Phys. **71**, 3419 (1992).

[109] S. Blügel, T. Brückel, and C. M. Scneider, *Magnetism goes Nano: Electron Correlations, Spin Transport, Molecular Magnetism* (Forschungszentrum Jülich GmbH, Institut für Festkörperforschung , 2005).

[110] M. Respaud *et al.*, Phys. Rev. B **57**, 2925 (1998).

[111] J. Espinosa, H. Shi, and D. Lederman, J. Appl. Phys. **97**, 10B310 (2005).

[112] P. Dai *et al.*, Solid State Comm. **100**, 865 (1996).

[113] J. B. Goodenough, Physical Review **100**, 564 (1955).

[114] D. C. Worledge *et al.*, J. Appl. Phys. **80**, 5158 (1996).

[115] S. H. Seo, H. C. Kang, H. W. Jang, and D. Y. Noh, Phys. Rev. B **71**, 12412 (2005).

[116] C. Heck, *Magnetic materials and their applications* (London Butterworths , 1974).

[117] P. A. Joy and S. K. Date, J. Magn. and Magn. Mater. **218**, 229 (2000).

[118] Y. S. Du *et al.*, J. Magn. and Magn. Mater. **297**, 88 (2006).

[119] J. C. Phillips, Physica C **340**, 292 (2000).

[120] E. Osquiguil *et al.*, Phys. Rev. B **49**, 3675 (1994).

[121] J. Hao, G. He, D. Lu, and H.-K. Wong, Mater. Lett. **46**, 225 (2000).